



Exploring the S-process History in the Galactic Disk: Cerium Abundances and Gradients in Open Clusters from the OCCAM/APOGEE Sample

J. V. Sales-Silva¹, S. Daflon¹, K. Cunha^{1,2}, D. Souto³, V. V. Smith⁴, C. Chiappini⁵, J. Donor⁶, P. M. Frinchaboy⁶, D. A. García-Hernández^{7,8}, C. Hayes⁹, S. R. Majewski¹⁰, T. Masseron^{7,8}, R. P. Schiavon¹¹, D. H. Weinberg^{12,13}, R. L. Beaton¹⁴, J. G. Fernández-Trincado^{15,16}, H. Jönsson¹⁷, R. R. Lane¹⁸, D. Minniti^{19,20}, A. Manchado^{7,8,21}, C. Moni Bidin¹⁵, C. Nitschelm²², J. O’Connell²³, and S. Villanova²³

¹ Observatório Nacional/MCTIC, R. Gen. José Cristino, 77, 20921-400, Rio de Janeiro, Brazil; joaovictor@on.br, joaovsaless@gmail.com

² Steward Observatory, University of Arizona, Tucson, AZ 85719, USA

³ Departamento de Física, Universidade Federal de Sergipe, Av. Marechal Rondon, S/N, 49000-000 São Cristóvão, SE, Brazil

⁴ Noirlab, Tucson, AZ 85719, USA

⁵ Leibniz-Institut für Astrophysik Potsdam (AIP), An der Sternwarte 16, D-14482 Potsdam, Germany

⁶ Department of Physics & Astronomy, Texas Christian University, TCU Box 298840, Fort Worth, TX 76129, USA

⁷ Instituto de Astrofísica de Canarias (IAC), E-38205 La Laguna, Tenerife, Spain

⁸ Universidad de La Laguna (ULL), Departamento de Astrofísica, E-38206 La Laguna, Tenerife, Spain

⁹ Department of Astronomy, University of Washington, Box 351580, Seattle, WA 98195, USA

¹⁰ Department of Astronomy, University of Virginia, Charlottesville, VA 22904-4325, USA

¹¹ Astrophysics Research Institute, Liverpool John Moores University, Liverpool, L3 5RF, UK

¹² Department of Astronomy & Center for Cosmology and AstroParticle Physics, The Ohio State University, Columbus, OH 43210, USA

¹³ Institute for Advanced Study, Princeton, NJ 08540, USA

¹⁴ The Carnegie Observatories, 813 Santa Barbara Street, Pasadena, CA 91101, USA

¹⁵ Instituto de Astronomía, Universidad Católica del Norte, Av. Angamos 0610, Antofagasta, Chile

¹⁶ Instituto de Astronomía y Ciencias Planetarias, Universidad de Atacama, Copayapu 485, Copiapó, Chile

¹⁷ Materials Science and Applied Mathematics, Malmö University, SE-205 06 Malmö, Sweden

¹⁸ Centro de Investigación en Astronomía, Universidad Bernardo O’Higgins, Avenida Viel 1497, Santiago, Chile

¹⁹ Departamento de Ciencias Físicas, Facultad de Ciencias Exactas, Universidad Andres Bello, Av. Fernandez Concha 700, Las Condes, Santiago, Chile

²⁰ Vatican Observatory, I-00120 Vatican City State, Italy

²¹ Instituto de Astrofísica de Canarias, C. Vía Láctea, s/n, 38205 San Cristóbal de La Laguna, Santa Cruz de Tenerife, Spain

²² Centro de Astronomía (CITEVA), Universidad de Antofagasta, Avenida Angamos 601, Antofagasta 1270300, Chile

²³ Departamento de Astronomía, Casilla 160-C, Universidad de Concepción, Concepción, Chile

Received 2021 August 31; revised 2021 November 11; accepted 2021 November 23; published 2022 February 21

Abstract

The APOGEE Open Cluster Chemical Abundances and Mapping survey is used to probe the chemical evolution of the s-process element cerium in the Galactic disk. Cerium abundances were derived from measurements of Ce II lines in the APOGEE spectra using the Brussels Automatic Code for Characterizing High Accuracy Spectra in 218 stars belonging to 42 open clusters. Our results indicate that, in general, for ages < 4 Gyr, younger open clusters have higher $[\text{Ce}/\text{Fe}]$ and $[\text{Ce}/\alpha\text{-element}]$ ratios than older clusters. In addition, metallicity segregates open clusters in the $[\text{Ce}/\text{X}]$ -age plane (where X can be H, Fe, or the α -elements O, Mg, Si, or Ca). These metallicity-dependent relations result in $[\text{Ce}/\text{Fe}]$ and $[\text{Ce}/\alpha]$ ratios with ages that are not universal clocks. Radial gradients of $[\text{Ce}/\text{H}]$ and $[\text{Ce}/\text{Fe}]$ ratios in open clusters, binned by age, were derived for the first time, with $d[\text{Ce}/\text{H}]/dR_{\text{GC}}$ being negative, while $d[\text{Ce}/\text{Fe}]/dR_{\text{GC}}$ is positive. $[\text{Ce}/\text{H}]$ and $[\text{Ce}/\text{Fe}]$ gradients are approximately constant over time, with the $[\text{Ce}/\text{Fe}]$ gradient becoming slightly steeper, changing by $\sim +0.009 \text{ dex kpc}^{-1} \text{ Gyr}^{-1}$. Both the $[\text{Ce}/\text{H}]$ and $[\text{Ce}/\text{Fe}]$ gradients are shifted to lower values of $[\text{Ce}/\text{H}]$ and $[\text{Ce}/\text{Fe}]$ for older open clusters. The chemical pattern of Ce in open clusters across the Galactic disk is discussed within the context of s-process yields from asymptotic giant branch (AGB) stars, gigayear time delays in Ce enrichment of the interstellar medium, and the strong dependence of Ce nucleosynthesis on the metallicity of its AGB stellar sources.

Unified Astronomy Thesaurus concepts: Galaxy evolution (594); Galaxy abundances (574); Milky Way disk (1050); Open star clusters (1160); S-process (1419)

1. Introduction

The elements heavier than the iron-peak elements are produced mostly via neutron captures onto atomic nuclei; in general, two distinct processes can account for the abundances of most of the heavy elements, with one process involving slow neutron capture rates, the s-process, and one driven by very rapid neutron capture rates, the r-process (Burbidge et al. 1957;

Käppeler et al. 2011). The r-process elements are mainly synthesized in merging neutron stars (Thielemann et al. 2017). The production of s-process elements, on the other hand, can be divided into three components, based upon analyses of solar and solar system abundances: a weak s-process component (nickel to strontium, $60 \lesssim A \lesssim 90$) produced in massive stars (Pignatari et al. 2010); a strong s-process component, terminating in ^{208}Pb , synthesized in low-metallicity asymptotic giant branch (AGB) stars (Gallino et al. 1998), and finally a main s-process component ($A > 90$, which includes cerium) from low- and intermediate-mass AGB stars (Lugaro et al. 2003). Although the s- and r-processes contribute in parallel to



Original content from this work may be used under the terms of the [Creative Commons Attribution 4.0 licence](https://creativecommons.org/licenses/by/4.0/). Any further distribution of this work must maintain attribution to the author(s) and the title of the work, journal citation and DOI.

the abundance of a given heavy element, the study of s- or r-process-dominated elements enables the isolated analysis of each of these processes. In particular, the cerium (Ce) abundance in the solar system has been produced mainly by the s-process ($83.5\% \pm 5.9\%$ contributed by the s-process, Bisterzo et al. 2014), making Ce an ideal element for exploring the s-process history in stellar populations.

Understanding AGB yields is essential to correctly interpret the s-process chemical evolution of the Galaxy, because these stars are its principal producers. The s-process production in AGB stars depends on the efficiency of the formation of a ^{13}C pocket in thermally pulsing (TP) AGB stars, because the main-component s-process neutrons are produced by $^{13}\text{C}(\alpha, n)^{16}\text{O}$.²⁴ These ^{13}C nuclei result from the mixing of H (protons) from the convective envelope of a TP AGB star into the shell H- and ^4He -burning regions, where the reaction $^{12}\text{C}(p, \gamma)^{13}\text{N}(\beta^+, \nu)^{13}\text{C}$ occurs. The mixing of protons from the convective envelope into the shell-burning regions of TP AGB stars depends upon such quantities as the metallicity, initial stellar mass, rotation, or magnetic fields (Gallino et al. 2006; Piersanti et al. 2013; Bisterzo et al. 2014; Cristallo et al. 2015; Battino et al. 2019; Vescovi et al. 2020; see also Karakas & Lattanzio 2014 for a review). This production site, with many variables, highlights the complexity involved in understanding the chemical evolution of the s-process elements produced by AGB stars. In this context, open clusters are crucial to unraveling this complicated panorama because they provide well-determined distances and ages.

In the last decade, large spectroscopic surveys (APOGEE, Gaia-ESO, and GALAH: Gilmore et al. 2012; Majewski et al. 2017; De Silva et al. 2015) have provided chemical abundances in large samples of open clusters through high-resolution spectroscopy, revealing details about the chemical evolution of the Galaxy. Along this line, Donor et al. (2020) performed a chemical analysis of Fe, α , K, Na, Al, and iron-peak elements using the sample of 128 open clusters from the Open Cluster Chemical Abundances and Mapping (OCCAM) survey from the Sloan Digital Sky Survey (SDSS) IV (Blanton et al. 2017) Apache Point Observatory Galactic Evolution Experiment 2 (APOGEE 2; Majewski et al. 2017) Data Release 16 (DR16; Holtzman et al. 2015; Nidever et al. 2015; Jönsson et al. 2020). Some of their main results included reliable Galactic abundance gradients for 16 elements and the evolution of $[X/\text{Fe}]$ gradients as a function of age for some elements, although the analysis of Ce was not included in Donor et al. (2020) due to the imprecision of Ce abundances in the APOGEE DR16 database. This larger uncertainty in the Ce abundances occurred due to the use of only one Ce II absorption line in DR16. In this study we extend the list of elements analyzed in the OCCAM sample to include cerium, using seven Ce II absorption lines in the APOGEE spectra, as discovered and studied by Cunha et al. (2017).

The abundance of s-process elements in the Galactic disk has been the subject of intense study in recent years (e.g., using open clusters: D’Orazi et al. 2009; Maiorca et al. 2011; Yong et al. 2012; Magrini et al. 2018; Spina et al. 2021; as well as field stars: Battistini & Bensby 2016; Spina et al. 2018; Tautvaišienė et al. 2021; Horta et al. 2021; among others); the

relationship between abundance and age may not be the same for all s-process elements (Yong et al. 2012; Jacobson & Friel 2013). Some studies found an increase of the $[X/\text{Fe}]$ abundance ratio of s-process elements, mainly Ba, with decreasing age of the open clusters and field disk stars (D’Orazi et al. 2009; Maiorca et al. 2012; Spina et al. 2018, 2021). However, Spina et al. (2020) proposed that the overabundance of Ba in young stars could be related to activity and magnetic enhancements. Baratella et al. (2021) explored different possible scenarios to explain Ba overabundances that they found in young open clusters (up to +0.6 dex in open clusters with ages <200 Myr), including chromospheric activity, but found these scenarios were not sufficient to explain the Ba overabundances. It is noted that their $[\text{La}/\text{Fe}]$ abundances were approximately solar, leading them to suggest Ce (or La) as a better tracer of the s-process and their temporal evolution (especially at younger ages).

For cerium, Maiorca et al. (2011), Spina et al. (2018), and Casamiquela et al. (2021) found a clear growth of the $[\text{Ce}/\text{Fe}]$ ratio with decreasing age for open clusters and field stars. Magrini et al. (2018) and Delgado Mena et al. (2019) derived a lower correlation of the $[\text{Ce}/\text{Fe}]$ ratio with age for open clusters and field stars respectively, while Tautvaišienė et al. (2021) determined a flat trend for thin-disk stars. In addition, there was a metallicity dependence in the relationship between $[\text{Ce}/\text{Fe}]$ ratio and age for field dwarf stars and open clusters (Delgado Mena et al. 2019; Casamiquela et al. 2021). Here, we investigate the s-process history using the Ce abundances of the large and homogeneous sample of OCCAM to further probe trends in the Ce ratios with age. In addition, we also analyze the dependence of this relationship on metallicity, because this may be an important observational constraint for models of chemical evolution.

Meanwhile, large uncertainties in the ages of field stars raise interest in finding chemical ratios that can serve as universal clocks for these stars. The abundance ratios between the s-process and α -elements are one target in this search, because they are produced by stars having very different lifetimes (gigayears for stars producing s-process elements and megayears for those producing α -elements). The $[\text{Y}/\text{Mg}]$ ratio appeared as one major candidate for such a universal chemical clock in stars (da Silva et al. 2012; Nissen 2015; Feltzing et al. 2017; Jofré et al. 2020); however, recent studies indicate that the relationship between the $[\text{Y}/\text{Mg}]$ ratio and age is not universal and varies throughout the Galactic disk (Delgado Mena et al. 2019; Casali et al. 2020; Casamiquela et al. 2021; Magrini et al. 2021). From a sample of 80 solar twins in the solar neighborhood, Jofré et al. (2020) found trends for Ce/Mg and Si with age, indicating that these were good chemical clocks. In this study, we examine the relationship between age and the abundance ratio of Ce with various α -elements ($[\text{Ce}/\alpha]$ where α can be O, Mg, Si, or Ca) whose abundances have been determined in APOGEE/DR16. This analysis allows us to further probe whether the correlation between age and $[\text{Ce}/\alpha]$ is universal for open clusters.

In this paper, we also determine the $[\text{Ce}/\text{H}]$ and $[\text{Ce}/\text{Fe}]$ radial gradients (Section 4). The large sample of open clusters allows us to show the gradient binned by age, enabling us to explore the evolution of the Ce gradient over time. In Section 2, we present details of the sample, as well as the derivations of the Ce abundances. We also compare our results with those

²⁴ In the more massive AGB stars ($M > 4 M_{\odot}$), the free neutrons are produced instead by the $^{22}\text{Ne}(\alpha, n)^{25}\text{Mg}$ neutron source but only elements from the first-peak around Rb are overproduced (e.g., García-Hernández et al. 2006, 2013; van Raaij et al. 2012, and references therein).

obtained in DR16 and the literature (Section 3). Concluding remarks about our results are found in the last section.

2. Sample and Methodology

APOGEE is a high-resolution, near-infrared (1.514–1.696 μm , Wilson et al. 2019) spectroscopic survey that in the latest public release (DR16) provided a detailed spectral analysis of approximately 430,000 stars (Zasowski et al. 2017; Jönsson et al. 2020). The APOGEE observations are made with the 2.5 m telescopes at Apache Point Observatory (New Mexico, USA, Gunn et al. 2006) and at Las Campanas Observatory (La Serena, Chile, Bowen & Vaughan 1973). The OCCAM survey (Donor et al. 2020) used the atmospheric parameters and chemical abundances from DR16, which were obtained with the APOGEE Stellar Parameters and Abundances Pipeline (ASPCAP, García Pérez et al. 2016) and a customized line list (Smith et al. 2021). Stars in the OCCAM sample were classified as open cluster members based on radial velocities, proper motions, spatial location, and derived metallicities (Donor et al. 2020).

The OCCAM sample consists of 914 stars belonging to 128 open clusters. Donor et al. (2020) classified 71 of the APOGEE open clusters as high-quality clusters based on their color-magnitude diagram and the reliability of the ASPCAP abundance results. Donor et al. (2020) investigated metallicity gradients for Na, Al, K, α , and iron-peak elements. In this study, we add to that list of elements and investigate the s-process-dominated element Ce in the open clusters of the OCCAM sample.

Cunha et al. (2017) found eight measurable Ce II absorption lines in the APOGEE wavelength region. However, in DR16 the Ce abundances were estimated using only one Ce II absorption line (15784.8 Å) due to difficulties in fitting the other Ce II lines automatically with ASPCAP. In this study, we consider all Ce II lines from Cunha et al. (2017) to improve the reliability of the Ce abundances in the APOGEE open cluster stars. The $\log gf$ values of the Ce II lines used in our analysis are from Cunha et al. (2017) for the lines at 16376.5 Å and 16722.6 Å, and from Smith et al. (2021) for the lines at 15277.6 Å, 15784.8 Å, 15977.1 Å, 16327.3 Å, and 16595.2 Å.

The methodology adopted to derive Ce abundances relies on χ^2 -squared fits between observed and synthetic spectra made from the Brussels Automatic Code for Characterizing High Accuracy Spectra (BACCHUS, Masseron et al. 2016). BACCHUS uses MARCS model atmospheres (Gustafsson et al. 2008) and the radiative transfer code Turbospectrum (Alvarez & Plez 1998; Plez 2012), which is exactly the machinery used in ASPCAP for DR16, and so makes the analysis self-consistent. Because C, N, and O abundances influence Ce II absorption lines in the APOGEE spectral region, we adopted the DR16 (uncalibrated) C, N, and O abundances along with the atmospheric parameters (T_{eff} , $\log g$, ξ , and $[\text{Fe}/\text{H}]$) to compute the syntheses in the Ce II line regions. The ASPCAP pipeline determines the atmospheric parameters and abundances automatically through best fits between the synthetic and observed spectra for the entire APOGEE region (Jönsson et al. 2020).

The Ce II lines in the APOGEE spectra can be weak and quite blended depending on the atmospheric parameters and chemical abundances of the studied stars (Cunha et al. 2017). We verified that giants hotter than 5000 K show Ce II lines with small equivalent widths, as also indicated by

Cunha et al. (2017), while giants cooler than 4000 K present Ce II lines strongly blended with molecular bands. Thus, we selected only giant stars ($\log g < 3.70$ dex) with 4000 K $< T_{\text{eff}} < 5000$ K from the OCCAM sample. After a careful inspection of the seven Ce II lines (see Table 4 in the Appendix) in each of the spectra of all targets, the final sample analyzed was reduced to 218 stars belonging to 42 open clusters; those were the stars from the high-quality OCCAM sample for which we could derive good Ce abundances with BACCHUS. We show in Figure 1 an example of the spectral syntheses and best-fit abundances for the five Ce II lines used to determine the Ce abundance of the star 2M20554232+5106153 from Berkeley 53. The individual Ce II lines and derived abundances for the sample stars are in Table 4. For completion, we also present the atmospheric parameters used in the computations of the spectral syntheses, which are the uncalibrated values from DR16. All cluster stars in our sample are red giants to minimize systematic errors and any possible effects of atomic diffusion (Souto et al. 2018, 2019) in the abundances. To verify trends due to possible non-LTE effects or other systematic errors in the analysis, we show in Figures 2 and 3 $[\text{Ce}/\text{Fe}]$ as a function of $\log g$ and T_{eff} , respectively, for the four open clusters with the largest numbers of stars analyzed (NGC 2158, NGC 2682, NGC 6791, and NGC 6819). The general behavior of the Ce abundance with T_{eff} or $\log g$ is reasonably constant, with the modulus of the slope ≤ 0.06 dex dex $^{-1}$ in the $[\text{Ce}/\text{H}]$ - $\log g$ plane and ≈ 0.00 dex K $^{-1}$ in the $[\text{Ce}/\text{H}]$ - T_{eff} plane.

The parameters of the open clusters adopted in this study are in Table 1. We present the average Ce abundances and the respective $[\text{Ce}/\text{H}]$ and $[\text{Ce}/\text{Fe}]$ ratios obtained for each studied cluster; we adopted the solar abundance of Grevesse et al. (2007), which is the same abundance scale used in DR16 chemical abundances. The ages and galactocentric distances for the open clusters were taken from Cantat-Gaudin et al. (2020), except for Berkeley 43 and FSR 0394, for which there were no estimates in that study. We use the values from Kharchenko et al. (2013) instead, given that Cantat-Gaudin et al. (2020) find generally good agreement with the age and distance estimates from Kharchenko et al. (2013).

We selected two sample stars (2M05240941+2937217 and 2M20554232+5106153) with different atmospheric parameters as references to estimate the uncertainties in Ce abundances derived in this study. The errors in the Ce abundances were derived by varying each atmospheric parameter independently by its typical estimated uncertainty: T_{eff} by +90 K, $\log g$ by +0.2 dex, ξ by +0.25 km s $^{-1}$ and $[\text{Fe}/\text{H}]$ by +0.1. In addition, we estimated the abundance uncertainties due to the synthetic fits of the Ce lines. We estimate the final errors by adding quadratically the uncertainties relative to each atmospheric parameter and synthetic fit. We show the uncertainties regarding the two stars in Table 2.

3. Comparison with DR16 and Optical Results from the Literature

We compare the Ce abundance results obtained in this study with those estimated in DR16. The reader is reminded that the Ce abundances from DR16 were derived with the ASPCAP pipeline and were based on a single Ce II line at 15784.8 Å. The average difference between our results and those from DR16 has a small offset but a significant standard deviation, $\Delta([\text{Ce}/\text{H}]_{\text{this study}} - [\text{Ce}/\text{H}]_{\text{DR16}}) = 0.05 \pm 0.16$, possibly indicating that the DR16 results have larger internal errors (Jönsson

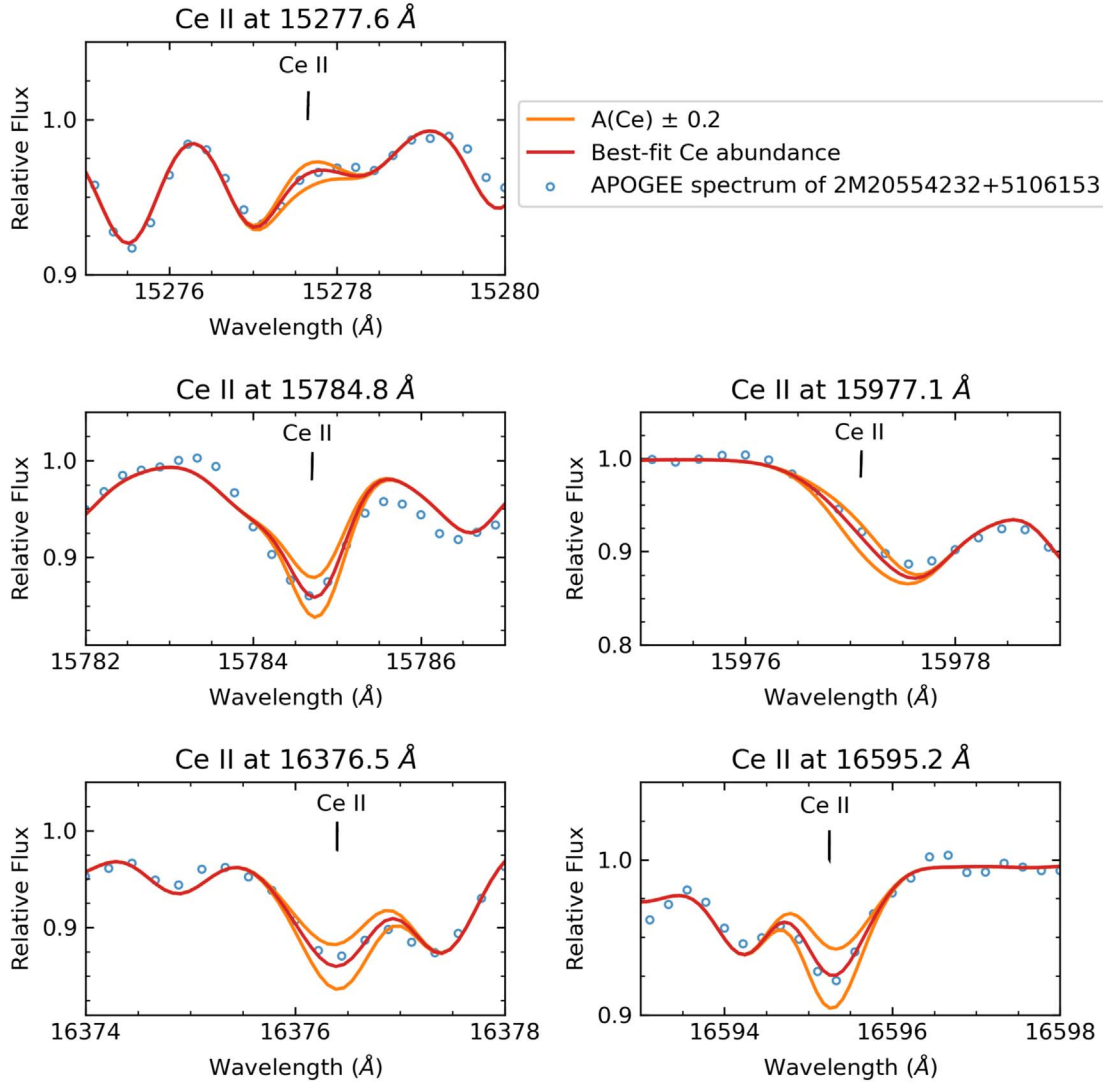


Figure 1. Observed (open blue circles) and synthetic spectra (solid lines) in the region of the five Ce II lines used to determine the Ce abundance of the Berkeley 53 red giant 2M20554232+5106153. Each panel shows one Ce II line and three synthetic spectra, with one synthesis representing the best-fit Ce abundance (red lines) and the others with $A(\text{Ce}) \pm 0.2$ dex (orange lines).

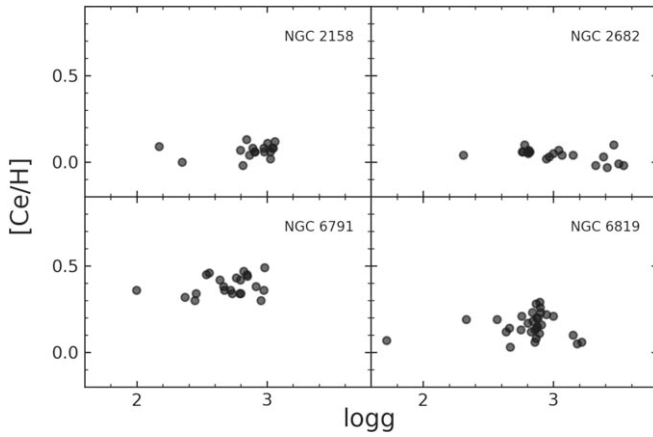


Figure 2. $[\text{Ce}/\text{H}]$ vs. surface gravity ($\log g$) for the stars in the open clusters NGC 2158, NGC 2682, NGC 6791, and NGC 6819, which are the ones having the largest numbers of stars analyzed. The OCCAM targets were selected to have $\log g$ less than 3.70; dwarf stars were not considered.

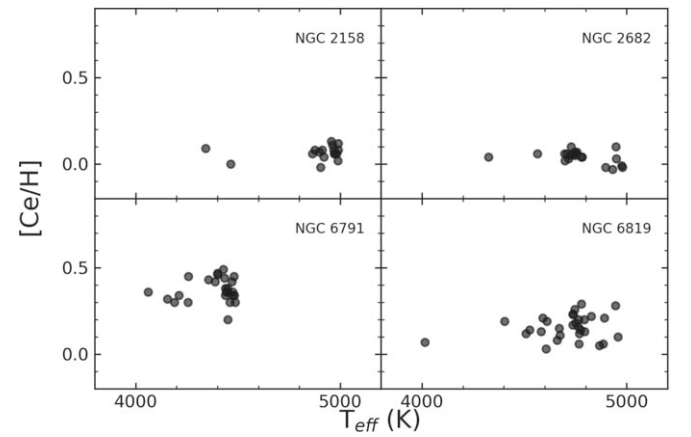


Figure 3. $[\text{Ce}/\text{H}]$ vs. T_{eff} for the studied stars that are members of the open clusters NGC 2158, NGC 2682, NGC 6791, and NGC 6819. Ce abundances were measured in the effective temperature interval between roughly 4000 and 5000 K. In general, there are no significant trends in $A(\text{Ce})$ with T_{eff} .

Table 1
Cluster Parameters and Abundance Ratios Used in This Study

Cluster	log(age/yr)	R_{GC} (kpc)	n_{star}	[Fe/H]	σ_{Fe}	$A(Ce)$	σ_{Ce}	[Ce/H]	[Ce/Fe]
Basel 11b	8.36	10.121	1	-0.004	...	1.940	...	0.240	0.244
Berkeley 17	9.86	11.668	7	-0.164	0.026	1.633	0.051	-0.067	0.097
Berkeley 19	9.34	14.890	1	-0.323	...	1.640	...	-0.060	0.263
Berkeley 20	9.68	16.320	1	-0.398	...	1.440	...	-0.260	0.138
Berkeley 29	9.49	20.577	1	-0.450	...	1.460	...	-0.240	0.210
Berkeley 43	8.79	7.120	1	0.026	...	2.020	...	0.320	0.294
Berkeley 53	8.99	9.026	6	-0.084	0.023	1.875	0.041	0.175	0.259
Berkeley 66	9.49	12.349	2	-0.159	0.031	1.770	0.014	0.070	0.229
Berkeley 98	9.39	9.788	1	0.004	...	1.780	...	0.080	0.076
BH 211	8.63	6.520	1	0.187	...	2.070	...	0.370	0.183
Collinder 220	8.37	8.080	1	-0.077	...	2.000	...	0.300	0.377
Czernik 21	9.41	12.349	2	-0.322	0.008	1.630	...	-0.070	0.252
Czernik 30	9.46	13.779	2	-0.396	0.008	1.505	0.021	-0.195	0.201
FSR 0394	9.20	10.500	2	-0.096	0.003	1.860	...	0.160	0.256
IC 1369	8.46	8.948	3	-0.079	0.037	1.917	0.032	0.217	0.296
IC 166	9.12	12.418	1	-0.086	...	1.860	...	0.160	0.246
King 2	9.61	13.264	1	-0.359	...	1.530	...	-0.170	0.189
King 5	9.01	10.526	1	-0.156	...	1.820	...	0.120	0.276
King 7	8.35	11.194	4	-0.160	0.024	1.978	0.052	0.278	0.438
NGC 1193	9.71	12.705	2	-0.334	0.004	1.510	0.071	-0.190	0.144
NGC 1245	9.08	11.118	1	-0.139	...	1.810	...	0.110	0.249
NGC 1798	9.22	13.266	6	-0.262	0.013	1.710	0.046	0.010	0.272
NGC 188	9.85	9.285	10	0.100	0.015	1.814	0.085	0.114	0.014
NGC 1907	8.77	9.947	1	-0.078	...	1.930	...	0.230	0.308
NGC 2158	9.19	12.617	17	-0.211	0.023	1.766	0.040	0.066	0.277
NGC 2204	9.32	11.344	6	-0.267	0.017	1.707	0.069	0.007	0.274
NGC 2243	9.64	10.584	8	-0.462	0.033	1.416	0.078	-0.284	0.178
NGC 2304	8.96	12.019	1	-0.142	...	1.850	...	0.150	0.292
NGC 2324	8.73	12.075	2	-0.181	0.027	1.845	0.021	0.145	0.326
NGC 2420	9.24	10.683	10	-0.190	0.033	1.698	0.051	-0.002	0.188
NGC 2682	9.63	8.964	21	0.021	0.018	1.741	0.036	0.041	0.020
NGC 4337	9.16	7.454	6	0.240	0.039	2.010	0.054	0.310	0.070
NGC 6705	8.49	6.464	10	0.121	0.039	2.028	0.032	0.328	0.207
NGC 6791	9.80	7.942	25	0.355	0.034	2.072	0.069	0.372	0.017
NGC 6811	9.03	8.203	1	-0.020	...	1.860	...	0.160	0.180
NGC 6819	9.35	8.027	30	0.055	0.030	1.857	0.070	0.157	0.102
NGC 752	9.07	8.669	1	-0.041	...	1.850	...	0.150	0.191
NGC 7789	9.19	9.432	14	-0.008	0.024	1.879	0.046	0.179	0.187
Ruprecht 147	9.48	8.046	1	0.138	...	1.840	...	0.140	0.002
SAI 116	8.10	7.528	2	0.161	0.011	2.040	0.071	0.340	0.179
Teutsch 84	9.02	6.018	1	0.214	...	2.000	...	0.300	0.086
Trumpler 5	9.63	11.211	3	-0.439	0.006	1.380	0.026	-0.320	0.119

Note. The $A(Ce)$ column shows the mean Ce abundance obtained in our study using BACCHUS. The galactocentric distance and age of the open clusters were obtained from Cantat-Gaudin et al. (2020). We used DR16 values to determine the average metallicity for each cluster.

et al. 2020). In Figure 4, we present violin plot distributions for the [Ce/H] abundances of the open clusters NGC 2158, NGC 2682, NGC 6791, and NGC 6819 obtained in this study (shown in red) and in DR16 (shown in blue). It is clear that, although the median abundance value for each cluster is not significantly offset, the Ce abundances derived here show much less internal dispersion than in DR16. Such small dispersions are expected under the paradigm that stars in open clusters do not show variations in chemical content.

Most previous studies in the literature derived Ce abundances for relatively small samples of open cluster (fewer than 10) using high-resolution optical spectra (e.g., Reddy et al. 2012, 2013; Santrich et al. 2013; Mishenina et al. 2015; Peña Suárez et al. 2018). Larger samples have been investigated in Maiorca et al. (2011), Magrini et al. (2018), and Casamiquela et al. (2021). A comparison of the Ce abundance results for the open clusters in

this study with the literature is presented in Figure 5, where we show the differences in the mean [Ce/H] values obtained (this study – other studies) for the open clusters labeled on the x -axis of the figure. The average differences in Ce abundance from the studies of Maiorca et al. (2011), Magrini et al. (2018), and Casamiquela et al. (2021) are respectively $\Delta[Ce/H] = 0.03 \pm 0.10$, 0.08 ± 0.12 , and 0.23 ± 0.06 . These indicate that there are small, or not significant, abundance offsets with the results from the first two studies when compared to ours, while with the recent study of Casamiquela et al. (2021) there is a more significant offset. For the well studied solar-metallicity open cluster NGC 2682 (or M67), for example, the Ce abundances obtained by Maiorca et al. (2011) ($[Ce/H] = 0.06 \pm 0.05$) and Magrini et al. (2018) ($[Ce/H] = 0.01 \pm 0.03$) are roughly solar or even so slightly enhanced, and quite similar to our [Ce/H] value of 0.04 ± 0.04 , while the result in

Table 2
Ce Abundance Uncertainties for 2M05240941+2937217 and 2M20554232+5106153

Star	ΔT_{eff} +90 K	$\Delta \log g$ +0.2	$\Delta \xi$ +0.25 km s ⁻¹	$\Delta [\text{Fe}/\text{H}]$ +0.1	$\Delta A(\text{Ce})_{\text{synth}}$	$(\sum \sigma^2)^{1/2}$
2M05240941+2937217	+0.06	+0.09	-0.05	+0.06	+0.06	0.15
2M20554232+5106153	+0.05	+0.09	-0.03	+0.02	+0.05	0.12

Note. Each column gives the variation in the abundance caused by the change in T_{eff} , $\log g$, ξ , or $[\text{Fe}/\text{H}]$. $\Delta A(\text{Ce})_{\text{synth}}$ indicates the abundance uncertainties due to the synthetic fits of the Ce lines. The last column gives the compounded uncertainty.

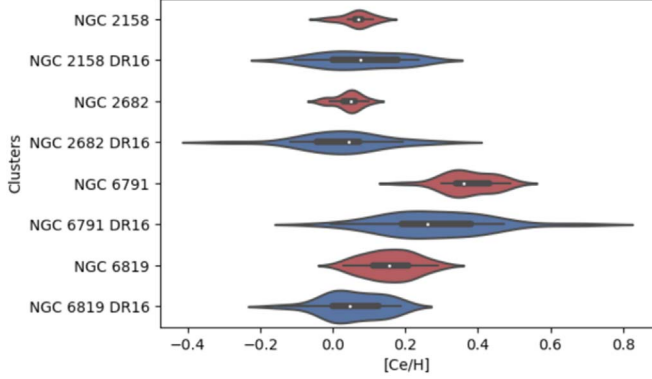


Figure 4. $[\text{Ce}/\text{H}]$ distribution for the open clusters NGC 2158, NGC 2682, NGC 6791, and NGC 6819. The red sequences represent our $[\text{Ce}/\text{H}]$ results while the blue sequences show the DR16 values for the four clusters. White dots in the distribution indicate the median, while the thick bar represents the interquartile range and the thin bar shows the 95% confidence interval. Wider regions of the distribution represent a higher probability that a star will have that $[\text{Ce}/\text{H}]$ value.

Casamiquela et al. (2021) is cerium-poor, $[\text{Ce}/\text{H}] = -0.16 \pm 0.03$. On the other hand, there are significant differences between our Ce abundances and those obtained for NGC 2324 in Maiorca et al. (2011) and for NGC 6705 in Magrini et al. (2018), with our $[\text{Ce}/\text{H}]$ values being higher by 0.17 and 0.28 dex, respectively. For NGC 2324 there are no other Ce abundance determinations available in the literature for further comparisons, although it is worth noting that D’Orazi et al. (2009) found a high Ba abundance (another heavy s-process-dominated element) in the open cluster NGC 2324 ($[\text{Ba}/\text{H}] = 0.49$), which would be generally in line with our Ce enrichment result for this cluster.

4. Ce Abundance Trends

4.1. The $[\text{Ce}/\text{Fe}]-[\text{Fe}/\text{H}]$ Plane

In Figure 6, we show the results for $[\text{Ce}/\text{Fe}]$ ratio as a function of $[\text{Fe}/\text{H}]$ for the open cluster sample studied here. In the top panel, we present our results as filled red circles while the results from the literature are shown as orange symbols (triangles, Maiorca et al. 2011; circles, Magrini et al. 2018; squares, other optical studies of open clusters: Reddy et al. 2012, 2013; Santrich et al. 2013; Mishenina et al. 2015; Peña Suárez et al. 2018). As violet circles, we show results on open clusters from Casamiquela et al. (2021), which have a significant offset when compared to our Ce abundances (see Figure 5). We also show, for comparison, results for dwarf stars (gray circles, Reddy et al. 2003, 2006; Mishenina et al. 2013; Bensby et al. 2014; Battistini & Bensby 2016; Fishlock et al. 2017), and red giant stars from the Galactic disk (green circles, Forsberg et al. 2019). The main feature is that the Ce

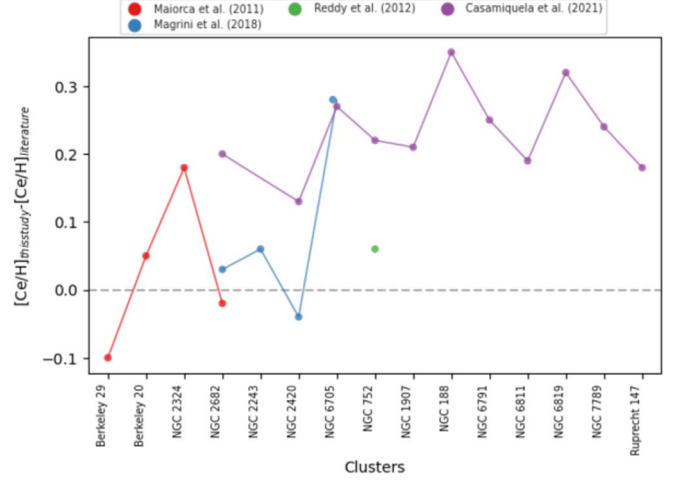


Figure 5. Comparison of the mean $[\text{Ce}/\text{H}]$ abundances for the clusters obtained here from the near-infrared APOGEE spectra with results from high-resolution optical spectroscopy from Maiorca et al. (2011) (red circles), Reddy et al. (2012) (green circle), Magrini et al. (2018) (blue circles), and Casamiquela et al. (2021) (purple circles) for the open clusters in common.

abundance results for open clusters in all studies generally overlap in the $[\text{Ce}/\text{Fe}]-[\text{Fe}/\text{H}]$ plane; $[\text{Ce}/\text{Fe}]$ increases as the metallicity decreases, with a possible downturn in the trend at roughly -0.2 in $[\text{Fe}/\text{H}]$.

The chemical pattern for the open clusters is found to be generally overabundant in the $[\text{Ce}/\text{Fe}]$ ratio when compared to most disk stars (giants and dwarfs) in the same metallicity range. Ba, another s-process-dominated element, also shows an overabundance in open clusters when compared to field disk stars (Yong et al. 2012). The field stars being systematically older than the open clusters may contribute to this difference, as pointed out by Yong et al. (2012).

In the lower panel of Figure 6, we show the studied open cluster sample but now with color representing log age (the age in the color bar shown on the right side of the plot). It is apparent that younger open clusters show $[\text{Ce}/\text{Fe}]$ ratios greater than older open clusters in the same metallicity range. It is the older clusters in our sample that show a change of slope in $[\text{Ce}/\text{Fe}]$ at roughly $[\text{Fe}/\text{H}] \approx -0.2$; we note, however, that the open clusters with the lowest metallicities in our sample are all older.

The chemical evolution model of Prantzos et al. (2018), which considers the yields from low- and intermediate-mass stars, rotating massive stars, and an r-process component, finds a $[\text{Ce}/\text{Fe}]$ ratio ~ 0.03 at solar metallicity and a maximum $[\text{Ce}/\text{Fe}]$ value of 0.20 around $[\text{Fe}/\text{H}] = -0.3$, followed by a drop in $[\text{Ce}/\text{Fe}]$ ratio for lower metallicities (see Figure 16 in Prantzos et al. 2018); this evolution reproduces well the

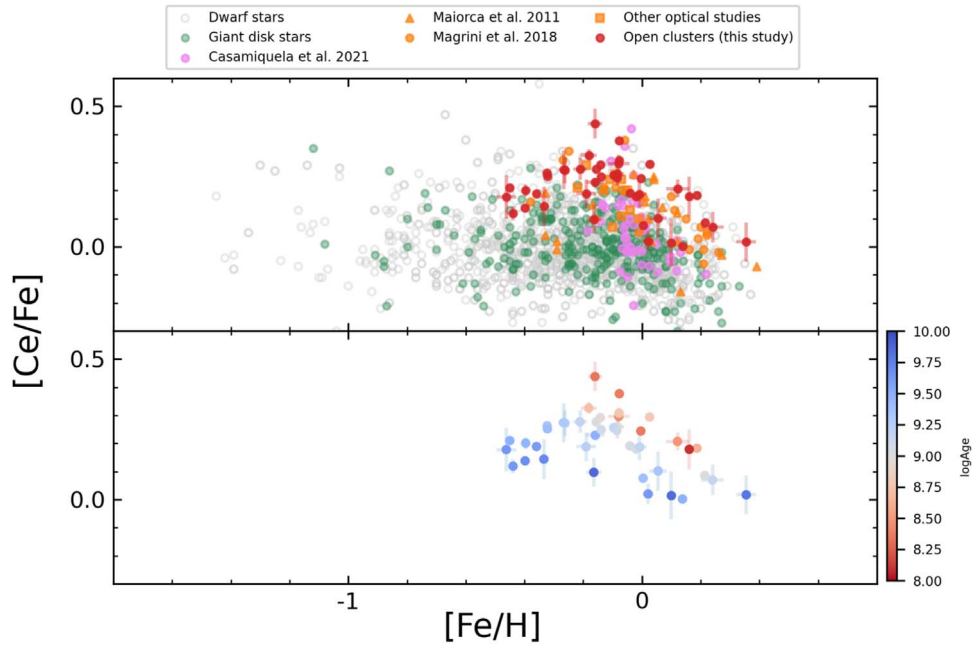


Figure 6. $[\text{Ce}/\text{Fe}]$ – $[\text{Fe}/\text{H}]$ plane for various stars in the Galactic disk. The top panel shows results for open clusters and field red giants and dwarfs. The filled red circles represent the open clusters from the OCCAM/APOGEE sample, while the orange symbols represent results for open clusters from optical studies in the literature: triangles from Maiorca et al. (2011), circles from Magrini et al. (2018), squares from Reddy et al. (2012, 2013), Santrich et al. (2013), Mishenina et al. (2015), and Peña Suárez et al. (2018). The violet circles represent results on open clusters from Casamiquela et al. (2021), which show an offset compared to our Ce abundances. The green symbols represent literature results for the disk giant stars from Forsberg et al. (2019) while gray symbols refer to dwarf disk stars from Reddy et al. (2003, 2006), Mishenina et al. (2013), Bensby et al. (2014), Battistini & Bensby (2016), and Fishlock et al. (2017). The bottom panel shows the $[\text{Ce}/\text{Fe}]$ results for open clusters in this study again, but with colors representing the cluster ages. Young open clusters ($\log \text{age} < 9.0$, or age < 1 Gyr; red circles) present a higher $[\text{Ce}/\text{Fe}]$ ratio than old open clusters in the same metallicity range.

relation between the $[\text{Ce}/\text{Fe}]$ ratio and metallicity shown by the old open clusters in our sample (dark blue circles in the lower panel of Figure 6), while young open clusters and the bulk of field giant stars from Forsberg et al. (2019) present, respectively, higher and lower $[\text{Ce}/\text{Fe}]$ values than that in the Prantzos et al. (2018) model.

In the metallicity range spanned by the Galactic open cluster population, AGB stellar model calculations indicate an increase in the production of heavy s-process elements (like Ce) with a decrease in $[\text{Fe}/\text{H}]$ (Gallino et al. 2006; Cristallo et al. 2015; Karakas & Lugaro 2016; Battino et al. 2019). The dependence of the s-process on $[\text{Fe}/\text{H}]$ is due to the ^{56}Fe acting as the seed nucleus for the synthesis of the s-process elements coupled with the reaction $^{13}\text{C}(\alpha, n)^{16}\text{O}$ being a primary source of neutrons. At low metallicities, the ratio of neutrons to Fe seed increases as $[\text{Fe}/\text{H}]$ decreases, resulting in larger neutron exposures with decreasing metallicity (Cristallo et al. 2009, 2011, 2015; Karakas & Lattanzio 2014; Karakas & Lugaro 2016).

4.2. The Chemical Evolution of Ce

4.2.1. $[\text{Ce}/\text{H}]$

To further explore trends in the cerium abundances with metallicity and age, in Figure 7 we plot the time evolution of $[\text{Ce}/\text{H}]$ and $[\text{Ce}/\text{Fe}]$ for the studied open cluster sample; the circles in the upper and middle panels of Figure 7 are now color-coded by metallicity, according to the color bar at the top of the figure. It is apparent that metallicity segregates the open clusters in the $[\text{Ce}/\text{X}]$ –age plane. In the case of $[\text{Ce}/\text{H}]$ (top panel), open clusters with larger metallicities (shown in blue) have larger $[\text{Ce}/\text{H}]$ values for the same age. In addition, $[\text{Ce}/\text{H}]$ in open clusters with similar metallicities exhibits a

correlation with age; open clusters with metallicities around 0.0 (light blue circles) show an increase in $[\text{Ce}/\text{H}]$ with decreasing age for clusters with age $\lesssim 4.0$ Gyr. A similar evolution of $[\text{Ce}/\text{H}]$ with age is found for open clusters of lower metallicities < -0.1 dex (red circles in Figure 7), but shifted to smaller $[\text{Ce}/\text{H}]$ values.

The oldest open clusters in this sample, with ages $>$ than 6 Gyr, are only three in number, making it challenging to reach meaningful conclusions about the $[\text{Ce}/\text{H}]$ evolution at early times in Galactic disk history. The behavior of the three oldest open clusters (age > 6 Gyr) in this sample (NGC 6791, NGC 188, and Berkeley 17) indicates that they do not follow the same $[\text{Ce}/\text{H}]$ sequence as the younger clusters. Open clusters with age > 6 Gyr and $[\text{Fe}/\text{H}] \leq 0.1$, for example, have $[\text{Ce}/\text{H}]$ values similar to the clusters that are between 2 and 3 Gyr old. The $[\text{Ce}/\text{H}]$ values result ultimately from the combination of AGB yields and the star formation rate at the birthplace of open clusters. As will be discussed below, the old clusters seem to follow the same lower sequence in $[\text{Ce}/\text{Fe}]$ as shown in the middle panel of the figure.

Being the most metal-rich ($[\text{Fe}/\text{H}] = +0.36$) as well as one of the oldest open clusters, NGC 6791 is worth discussing in comparison to the much younger, but also metal-rich ($[\text{Fe}/\text{H}] = +0.19$), open cluster BH 211. Both clusters have the highest $[\text{Ce}/\text{H}]$ abundance ($[\text{Ce}/\text{H}] = +0.37$ in both), yet they have very different ages. BH 211 is a very young (age = 0.42 Gyr; Cantat-Gaudin et al. 2020), metal-rich open cluster, whereas NGC 6791 is an old open cluster (age = 6.31 Gyr; Cantat-Gaudin et al. 2020) that is even more metal-rich. This simple comparison of these two clusters makes it evident that clusters having very different ages can reach similar $[\text{Ce}/\text{H}]$ values. The old age and chemical enrichment of NGC 6791

(very high $[\text{Fe}/\text{H}]$ and high $[\text{Ce}/\text{H}]$) suggest that this cluster was probably formed in a region with a high star formation rate. Observational studies of the interstellar medium indicate that regions of the inner disk are characterized by a higher star formation rate than regions of the outer disk (e.g. Misiriotis et al. 2006; Djordjevic et al. 2019). Our results for the $[\text{Ce}/\text{H}]$ gradient support an outward radial migration scenario of NGC 6791 from the innermost regions of the disk, as shown in the next subsection. Chemical abundance and dynamic studies of NGC 6791 also indicate radial migration to its current position (Jílková et al. 2012; Martínez-Medina et al. 2018; Villanova et al. 2018; Chen & Zhao 2020).

4.2.2. $[\text{Ce}/\text{Fe}]$

In addition to having a dependence on metallicity, stellar evolution models show that AGB yields are heavily dependent on stellar mass, with low-mass stars (around $2 \pm 1 M_{\odot}$ for $[\text{Fe}/\text{H}] \approx -1.0$) having the largest yields²⁵ (Cristallo et al. 2015). Low-mass stars may require a few gigayears to add their chemical products, such as the s-process elements, to the interstellar medium, resulting in a delay to the enrichment of the interstellar medium by the s-process elements from this source. The evolution of the $[\text{Ce}/\text{Fe}]$ ratio observed is in line with a delay between the enrichment caused by AGB stars and that caused by Type Ia supernovae. Figure 7 (middle and bottom panels) shows the $[\text{Ce}/\text{Fe}]$ ratio versus age for this sample. Open clusters with lower metallicities (red circles) have a higher $[\text{Ce}/\text{Fe}]$ ratio than clusters with higher metallicities (blue circles); this behavior is reversed when considering only $[\text{Ce}/\text{H}]$. The strong dependence of $[\text{Ce}/\text{H}]$ on the star formation rate (as shown by its gradient plotted in the next subsection) may explain the different behaviors for $[\text{Ce}/\text{H}]$ and $[\text{Ce}/\text{Fe}]$. For ages < 4 Gyr, the $[\text{Ce}/\text{Fe}]$ ratio increases with decreasing age of the open clusters in all metallicity regimes. This result is in agreement with previous studies from optical high-resolution spectroscopy for open clusters and field disk stars (e.g., Maiorca et al. 2011; Spina et al. 2018).

The open clusters can be segregated into two groups in the $[\text{Ce}/\text{Fe}]$ –age plane—those having $[\text{Fe}/\text{H}] \geq -0.1$ and $[\text{Fe}/\text{H}] < -0.1$ —and we compute the average $[\text{Ce}/\text{Fe}]$ in each gigayear bin for each group. In the lower panel of Figure 7, we show the average $[\text{Ce}/\text{Fe}]$ per bin along with the respective standard deviations, with the horizontal bars corresponding to the bin size. We note that when there is only one cluster in a bin we use the result for that cluster (square symbols in the lower panel of Figure 7). There seems to be an overall similar relation between the $[\text{Ce}/\text{Fe}]$ ratio and age in the two groups but shifted in $[\text{Ce}/\text{Fe}]$. For ages < 4 Gyr, we see an increase in the $[\text{Ce}/\text{Fe}]$ ratio with decreasing age. However, for ages > 4 Gyr, we have roughly a constant value of $[\text{Ce}/\text{Fe}]$ ratio with age, with $[\text{Ce}/\text{Fe}] \approx 0.0$ and ≈ 0.13 for the metal-rich ($[\text{Fe}/\text{H}] \geq -0.1$) and metal-poor ($[\text{Fe}/\text{H}] < -0.1$) open clusters, respectively.

In the bottom panel of Figure 7, we include linear fits in the $[\text{Ce}/\text{Fe}]$ –age plane as presented in studies by Spina et al. (2018), Magrini et al. (2018), and Delgado Mena et al. (2019).

²⁵ The nucleosynthesis predictions for low-mass AGB stars ($< 3\text{--}4 M_{\odot}$) generally agree quite well among the different AGB nucleosynthesis models/codes (e.g., FRUITY, Monash, ATON, NuGrid/MESA). The situation is very different for the higher-mass ($> 4 M_{\odot}$) AGB stars, where the model predictions are very dependent on the nucleosynthesis code used (see Karakas & Lugaro 2016, for a detailed discussion about the model predictions of different codes).

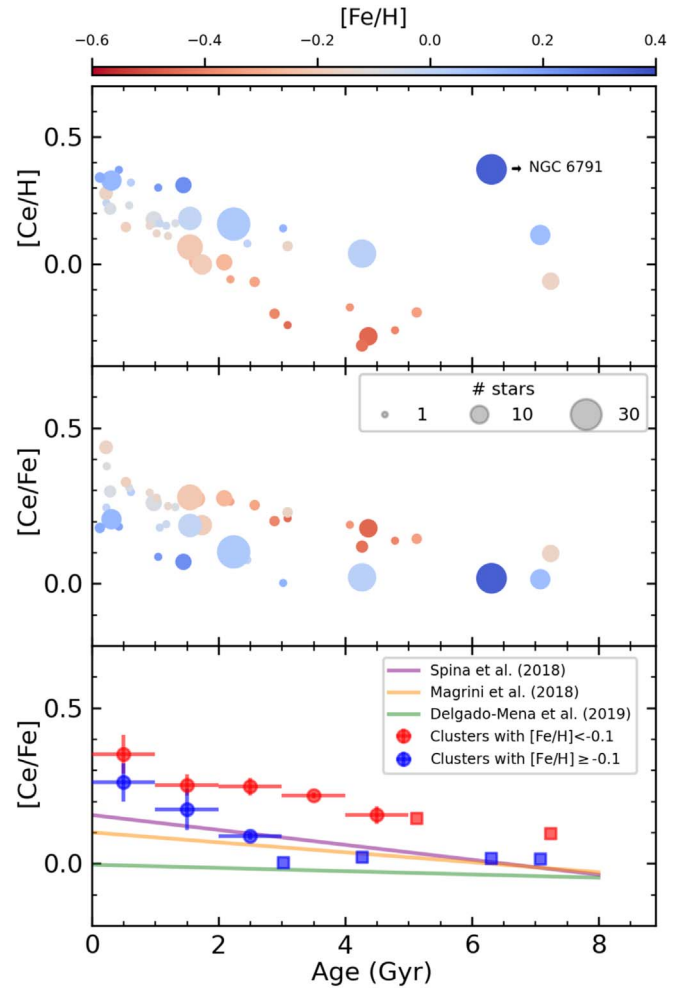


Figure 7. The evolution of $[\text{Ce}/\text{H}]$ and $[\text{Ce}/\text{Fe}]$ ratios for the studied open clusters as a function of their age. Top and middle panels: circles represent the mean $[\text{Ce}/\text{H}]$ and $[\text{Ce}/\text{Fe}]$ obtained for the open clusters, and their colors indicate the mean metallicities of the clusters, while their sizes symbolize the number of stars analyzed in each open cluster (see Table 1). Bottom panel: circles represent the average of the $[\text{Ce}/\text{Fe}]$ ratio for the open clusters at 1 Gyr bin and in two metallicity regimes. Red circles represent the mean using only open clusters with $[\text{Fe}/\text{H}] < -0.1$, while blue circles refer to the average for clusters with $[\text{Fe}/\text{H}] \geq -0.1$. Squares represent regions in 1 Gyr bins where we have only one open cluster. The purple, orange, and green lines represent the best linear fits obtained by Spina et al. (2018), Magrini et al. (2018), and Delgado Mena et al. (2019), respectively.

Spina et al. (2018) used a sample of 79 solar twin stars (having, by definition, $[\text{Fe}/\text{H}] \approx 0.0$) and derived an increase in the $[\text{Ce}/\text{Fe}]$ ratio with decreasing age, similar to the trend derived by Magrini et al. (2018), who used a sample of open clusters in the solar neighborhood (10) and a sample of thin-disk field stars with ages less than 8 Gyr. The trends from Spina et al. (2018) and Magrini et al. (2018) are similar, and track our overall results for the open clusters with $[\text{Fe}/\text{H}] \geq -0.1$, but for the older clusters we find a flat behavior of $[\text{Ce}/\text{Fe}]$ with age, with a transition at around 3–4 Gyr to increasing $[\text{Ce}/\text{Fe}]$ for younger clusters. At young ages, our results do diverge slightly from the simplified linear trends from Spina et al. (2018) and Magrini et al. (2018).

The linear trend from Delgado Mena et al. (2019) is flatter than those from both Spina et al. (2018) and Magrini et al. (2018), as well as the open cluster trends found here. For the thin-disk stars in their sample with ages less than 8 Gyr there is

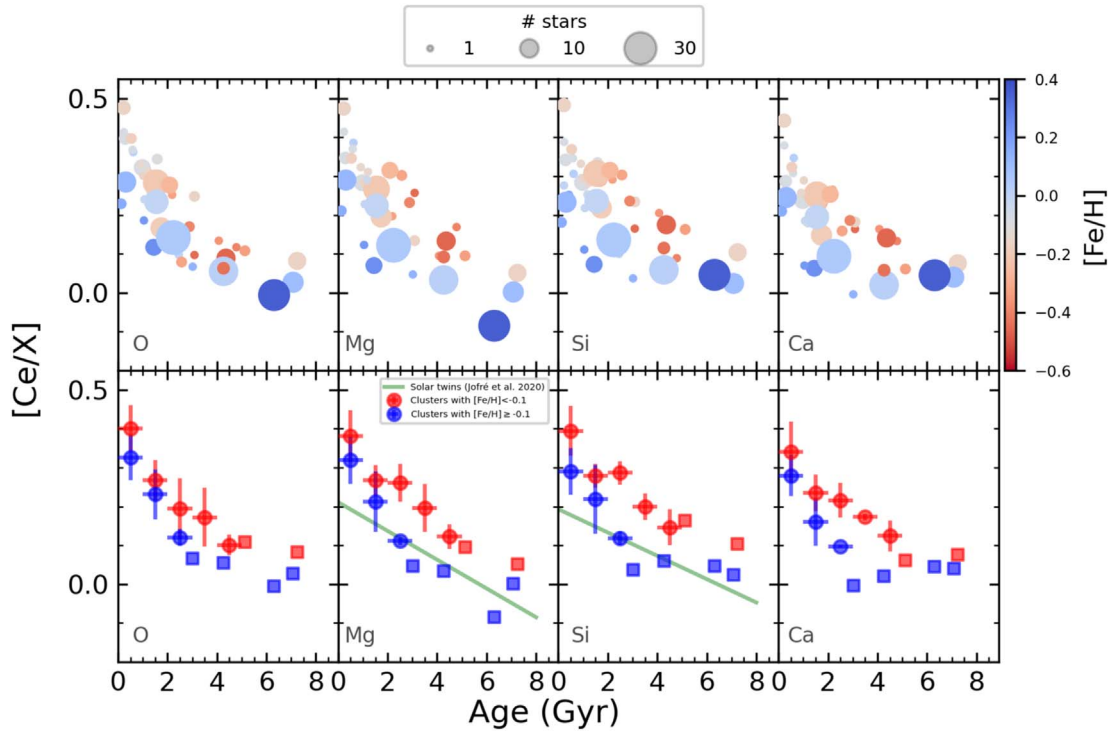


Figure 8. The evolution of the abundances of Ce relative to the abundances of the α -elements O, Mg, Si, and Ca as a function of cluster age. Top panels: circles represent the mean bracket abundance values for the open clusters. Circle colors indicate their mean metallicities. Circle sizes symbolize the number of stars analyzed in each open cluster (see Table 1). Bottom panels: the average of the Ce abundance relative to the α -elements as a function of open cluster age. The average values were computed for cluster ages within 1 Gyr bins, segregating the sample into two metallicity regimes. Red circles represent the mean using only open clusters with $[\text{Fe}/\text{H}] < -0.1$, while blue circles refer to the average for clusters with $[\text{Fe}/\text{H}] \geq -0.1$. Squares represent regions in 1 Gyr bins where we have only one open cluster. The green lines represent the best linear fits obtained by Jofré et al. (2020) for solar twins.

significant scatter that increases at young ages (their Figure 7), but Delgado Mena et al. (2019) find a distribution of $[\text{Ce}/\text{Fe}]$ that is approximately flat as a function of age with a mean $[\text{Ce}/\text{Fe}] \sim 0.0$ (see green line in the bottom panel of Figure 7). Their best-fit line to their data is not in good agreement with our results for the open clusters with $[\text{Fe}/\text{H}] < -0.1$ (red circles). Although it is in better agreement with the open clusters with $[\text{Fe}/\text{H}] > -0.1$ (blue circles), there is more divergence for the younger clusters as $[\text{Ce}/\text{Fe}]$ rises for younger open cluster ages. We note that one difference between the field dwarfs from Delgado Mena et al. (2019) and the open clusters studied here is the lack of young open clusters with low values of $[\text{Ce}/\text{Fe}]$ (~ -0.1 to -0.2) that is seen in the disk population. Delgado Mena et al. (2019) also investigate the linear fits to thin-disk stars with different $[\text{Fe}/\text{H}]$ ranges. They find that the relationship between s-process abundances (including Ce) and age varies with metallicity, as also indicated by our results.

The change in the time evolution of the $[\text{Ce}/\text{Fe}]$ ratio with metallicity in open clusters highlights the dependence of the synthesis of s-process elements on the metallicity. Stellar evolution models indicate lower $[\text{X}/\text{Fe}]$ ratios of s-process elements in higher-metallicity AGB stars (Cristallo et al. 2015; Karakas & Lugaro 2016; Battino et al. 2019), corroborating our results.

4.2.3. $[\text{Ce}/\alpha]$

The s-process elements are mainly produced by low- and intermediate-mass stars that have longer lifetimes than high-mass stars, which are the source of the α -elements. The difference in their lifetimes has led to previous suggestions that s-process to

α -element ratios could serve as good chemical chronometers (e.g. da Silva et al. 2012; Nissen 2015; Feltzing et al. 2017). In this study, we seek to investigate whether the ratios of Ce to α -elements are universal clocks. In Figure 8, we show the evolution of $[\text{Ce}/\alpha]$ ratios with cluster age, using the O, Mg, Si, and Ca uncalibrated abundances from APOGEE DR16. Metallicity segregates the open clusters in the $[\text{Ce}/\alpha]$ -age plane (Figure 8). In general, clusters with lower metallicities have higher $[\text{Ce}/\alpha]$ ratios, although the trend of the $[\text{Ce}/\alpha]$ ratio with age is similar across the entire metallicity range: there is an increase in the $[\text{Ce}/\alpha]$ ratio with decreasing open cluster age.

As done previously for Fe (bottom panel of Figure 7), we also computed the average abundance ratios of Ce to α -elements in the same 1 Gyr bins and for the same two metallicity regimes (above and below $[\text{Fe}/\text{H}] = -0.1$); the behavior of $[\text{Ce}/\alpha]$ versus cluster age is shown in Figure 8 for the “low” (in red) and “high” (in blue) metallicity cluster groups. The average $[\text{Ce}/\alpha]$ ratios for the lower-metallicity ($[\text{Fe}/\text{H}] < -0.1$) open cluster group are shifted to higher values when compared to the high-metallicity group ($[\text{Fe}/\text{H}] \geq -0.1$), with average differences between these two metallicity groups of 0.07 ± 0.02 , 0.09 ± 0.04 , 0.11 ± 0.04 , and 0.10 ± 0.05 for $[\text{Ce}/\text{O}]$, $[\text{Ce}/\text{Mg}]$, $[\text{Ce}/\text{Si}]$, and $[\text{Ce}/\text{Ca}]$ ratios, respectively. These differences are approximately equal for all $[\text{Ce}/\alpha]$ abundance ratios.

Overall, the $[\text{Ce}/\alpha]$ ratio for all studied α -elements (O, Mg, Si and Ca) shows a similar dependence on age in both metallicity groups. For old open clusters with ages > 4 Gyr, there is an approximately constant relation of the $[\text{Ce}/\alpha]$ ratio with age also for both metallicity groups. (As previously mentioned, our sample of open clusters with age > 4 Gyr is small; however, there is a need to analyze a more robust open

cluster sample to confirm (or not) the constant evolution of $[\text{Ce}/\alpha]$ with time.) On the other hand, open clusters with age < 4 Gyr show an increase in the $[\text{Ce}/X]$ ratio with decreasing age in the two metallicity groups, a behavior that is reminiscent of that found for the $[\text{Ce}/\text{Fe}]$ ratio. Jofré et al. (2020) analyzed trends in the $[\text{Ce}/\text{Mg}]$ –age and $[\text{Ce}/\text{Si}]$ –age planes for the same sample of solar twin stars from Spina et al. (2018). In the bottom panel of Figure 8, we show their best-fit line obtained for their sample of solar twins in the solar neighborhood (solid green line). The overall trend is the same as the one found for the open clusters in general; there is a better agreement with those open clusters having $[\text{Fe}/\text{H}] \geq -0.1$, which is reasonable, because the solar twins have near-solar metallicity; however, although the general behavior is similar, our data may suggest a more complex behavior.

The increase in $[\text{Ce}/\alpha]$ and $[\text{Ce}/\text{Fe}]$ ratios is interpreted as a signature of the late chemical evolution of Ce. We note that the $[\text{Fe}/\alpha]$ values are generally within ~ 0.1 and show no significant trend with age for either the metal-rich or metal-poor subset. Therefore, the $[\text{Ce}/\alpha]$ –age trend provides information that cannot be obtained from the $[\alpha/\text{Fe}]$ ratio.

Finally, the results here indicate that the $[\text{Ce}/\alpha]$ –age ratio is not universal for open clusters, but, rather, is strongly dependent on metallicity, as also shown for the $[\text{Y}/\alpha]$ ratio (e.g., Delgado Mena et al. 2019; Magrini et al. 2021). Recently, Casali et al. (2020) and Magrini et al. (2021) indicated that the non-universality of the $[\text{s-process}/\alpha]$ –age– $[\text{Fe}/\text{H}]$ relation is caused by star formation history and s-process yields, with their metallicity dependence. In particular, Magrini et al. (2021) used models of the chemical evolution of the Galaxy that consider magnetic-buoyancy-induced mixing in AGB stars to explain the change in the relationship between $[\text{Y}/\text{Mg}]$ and age with metallicity observed in the open clusters from Magrini et al. (2018). Magrini et al. (2021) pointed out that the mixing triggered by magnetic fields may cause a change in s-process production and in its relationship with metallicity by changing the ^{13}C pocket (main source of s-process neutrons) inside the TP AGB stars. This scenario presented by Magrini et al. (2021) exposes the complexity that involves s-process nucleosynthesis and $[\text{Fe}/\text{H}]$. Homogeneous studies with a significant sample of objects with well-defined ages, such as the one presented here, are essential in testing the evolutionary models of AGB stars and unveiling the complex relationship between the s-process production and metallicity.

4.3. The Ce Abundance Gradient

Radial abundance gradients in the Galaxy provide information on the star formation rate and serve as observational constraints to models of chemical evolution. In particular, open clusters are essential pieces in studies of abundance gradients because their distances and ages are more accurate than those for field stars. In Figure 9, we show the $[\text{Fe}/\text{H}]$ (top panel) and $[\text{Ce}/\text{H}]$ (bottom panel) gradients for the studied open cluster sample, using the homogeneous distance estimates from Cantat-Gaudin et al. (2020). The studied open clusters cover the galactocentric distance range between 6.0 and 20.6 kpc, with all but two clusters having galactocentric distances less than 15 kpc (Table 1). We realized the best linear fits for the gradients using the maximum likelihood, with associated uncertainties being estimated through the Markov Chain Monte Carlo routine from the emcee Python package (Foreman-Mackey et al. 2013), as previously done in Donor et al. (2020) for $[\text{Fe}/\text{H}]$ gradients.

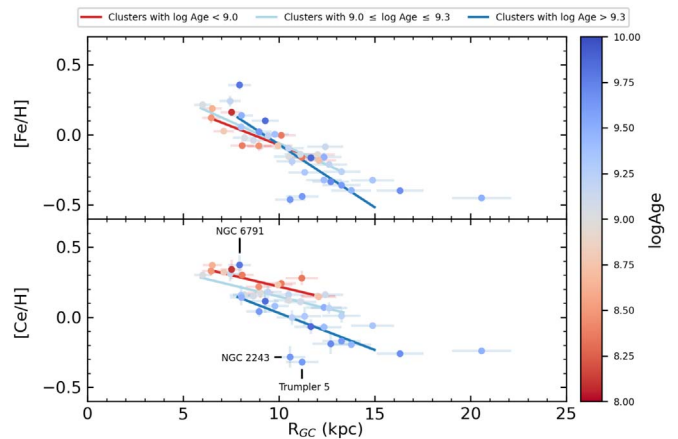


Figure 9. The $[\text{Fe}/\text{H}]$ (top panel) and $[\text{Ce}/\text{H}]$ (bottom panel) cluster mean abundances as a function of cluster galactocentric distance; the colors represent cluster age. Three gradients were computed for samples of open clusters segregated according to their age. In both panels, the linear fits shown as red, light blue, and dark blue lines correspond to open clusters with age < 1.0 Gyr, $1 \text{ Gyr} \leq \text{age} \leq 2 \text{ Gyr}$, and age > 2.0 Gyr, respectively. The fits were computed for $R_{\text{GC}} < 15$ kpc. There is an age segregation in $[\text{Ce}/\text{H}]$ as a function of galactocentric distance. In general, younger open clusters (red circles) show higher $[\text{Ce}/\text{H}]$ ratios than older clusters (blue circles) at a given galactocentric distance. The behavior of $[\text{Fe}/\text{H}]$ is different than that of $[\text{Ce}/\text{H}]$.

When considering the cluster sample having galactocentric distances $R_{\text{GC}} < 15$ kpc, we obtain a $[\text{Ce}/\text{H}]$ gradient of $-0.070 \pm 0.007 \text{ dex kpc}^{-1}$, approximately equal to our estimate for the $[\text{Fe}/\text{H}]$ gradient ($-0.071 \pm 0.008 \text{ dex kpc}^{-1}$), which, as expected, is close to the metallicity gradient found in Donor et al. (2020, $-0.068 \text{ dex kpc}^{-1}$) from the analysis of a larger number of open clusters from the OCCAM sample. This is also in agreement with the metallicity gradient from Spina et al. (2021, $-0.076 \text{ dex kpc}^{-1}$) obtained using a combination of APOGEE and GALAH results put on the same reference scale. Concerning $[\text{Ce}/\text{H}]$, the earlier study by Maiorca et al. (2011) found that $[\text{Ce}/\text{H}]$ decreases with galactocentric distance from the analysis of a sample of 19 open clusters, but that study did not compute a $[\text{Ce}/\text{H}]$ gradient.

In Figure 9, we now focus on gradients as a function of open cluster age. In both panels of the figure, the colors of the filled circles represent log age, according to the color bar. $[\text{Fe}/\text{H}]$ (top panel) and $[\text{Ce}/\text{H}]$ (bottom panel) gradients are obvious. First, it seems clear that there is an age segregation in the $[\text{Ce}/\text{H}]$ – R_{GC} plane: the younger the open cluster, the higher the $[\text{Ce}/\text{H}]$ value throughout the thin disk (over the entire R_{GC} range probed). A similar behavior is not seen for the $[\text{Fe}/\text{H}]$ – R_{GC} plane (top panel of the figure), because the populations do not segregate in this parameter space. In general, as discussed previously, the age segregation of Ce abundances may be due to late enrichment of Ce to the natal cloud.

Given the age segregation in the $[\text{Ce}/\text{H}]$ – R_{GC} plane, we now divide the open cluster sample into three populations and compute the gradients considering $R_{\text{GC}} < 15$ kpc: very young clusters with ages less than 1 Gyr, clusters with ages within the narrow range between 1 and 2 Gyr, and clusters older than 2 Gyr. The linear fits to the data in each case are shown in Figure 9 as red, light blue, and dark blue lines respectively. In Table 3, we present the radial abundance gradients (dex kpc^{-1}) binned by age for our open cluster sample with $R_{\text{GC}} < 15$ kpc. We find that the slopes of the linear fits in the $[\text{Ce}/\text{H}]$ – R_{GC} plane are approximately equal for the different age groups of the open clusters. Open clusters with age < 1 Gyr and $1 \text{ Gyr} \leq \text{age} \leq 2 \text{ Gyr}$ show a gradient of $-0.033 \pm 0.007 \text{ dex}$

Table 3
Radial Abundance Gradients (dex kpc^{-1}) and Intercept Coefficient of the Best Linear Fits Binned by Age for Open Clusters with $R_{\text{GC}} < 15 \text{ kpc}$

	#	R_{GC} (kpc) Range	[Fe/H]		[Ce/H]		[Ce/Fe]	
			$d[\text{Fe}/\text{H}]/dR_{\text{GC}}$	Intercept	$d[\text{Ce}/\text{H}]/dR_{\text{GC}}$	Intercept	$d[\text{Ce}/\text{Fe}]/dR_{\text{GC}}$	Intercept
All open clusters	40	$6.02 \leq R_{\text{GC}} \leq 14.89$	-0.071 ± 0.008	0.634 ± 0.082	-0.070 ± 0.007	0.614 ± 0.077	0.014 ± 0.007	0.061 ± 0.071
age < 1 Gyr	12	$6.46 \leq R_{\text{GC}} \leq 12.07$	-0.054 ± 0.011	0.462 ± 0.104	-0.033 ± 0.006	0.544 ± 0.061	0.018 ± 0.008	0.116 ± 0.79
1 Gyr \leq age \leq 2 Gyr	12	$6.02 \leq R_{\text{GC}} \leq 13.27$	-0.061 ± 0.010	0.552 ± 0.107	-0.033 ± 0.007	0.479 ± 0.078	0.027 ± 0.007	-0.058 ± 0.077
age > 2.0 Gyr	16	$7.94 \leq R_{\text{GC}} \leq 14.89$	-0.089 ± 0.018	0.825 ± 0.205	-0.053 ± 0.018	0.557 ± 0.198	0.035 ± 0.007	-0.258 ± 0.077

Note. We also show the number of open clusters (#) and the galactocentric distance range covered by each age sample.

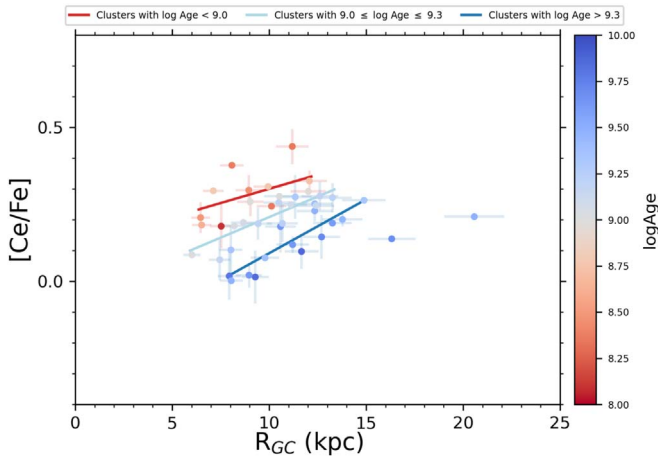


Figure 10. The $[\text{Ce}/\text{Fe}]$ gradients obtained for the studied open cluster sample. Three gradients were computed as in Figure 9. In general, younger open clusters (red circles) show higher $[\text{Ce}/\text{Fe}]$ ratios than older clusters (blue circles) at a given galactocentric distances.

kpc^{-1} , just slightly flatter than the gradient obtained for clusters with age > 2.0 Gyr ($-0.053 \pm 0.018 \text{ dex kpc}^{-1}$) but similar within the uncertainties.

The larger uncertainty in the best fit for the older group is caused by greater dispersion of this sample. We observed that three old open clusters (NGC 6791, Trumpler 5, and NGC 2243) present the highest residuals²⁶ of our sample (>0.22 dex), contributing to the imprecision of the linear fit of old clusters. The $[\text{Fe}/\text{H}]$ and $[\text{Ce}/\text{H}]$ gradients for the old open clusters without NGC 6791, Trumpler 5, and NGC 2243 are -0.081 ± 0.010 and -0.043 ± 0.011 , respectively, these being less uncertain but equal within the uncertainties to the gradients obtained considering the entire sample of old clusters. Probably these open clusters underwent a radial migration process. NGC 6791 is known to exhibit significant radial migration (Martínez-Medina et al. 2018; Villanova et al. 2018; Chen & Zhao 2020). Miglio et al. (2021) have identified a population of metal-rich red giant stars ($[\text{Fe}/\text{H}] > 0.2$) at the solar galactocentric distance with a chemical pattern and age similar to NGC 6791, indicating that these stars also likely suffered a radial migration from their birthplace to the solar neighborhood. NGC 2243 (age = 4.4 Gyr) and Trumpler 5 (age = 4.3 Gyr) have a very low value of $[\text{Ce}/\text{H}] \sim -0.3$; by sharing a very low $[\text{Ce}/\text{H}]$ they would seem to follow a potentially flatter gradient of the two old clusters that are found beyond 15 kpc. In general, radial migration of old open clusters is expected to be more significant than that of young open clusters due to longer exposure to the bar and spiral arm perturbations (Jílková et al. 2012; Chen & Zhao 2020).

Concerning iron, the metallicities and gradients obtained for the open cluster sample with $R_{\text{GC}} < 15$ kpc do not exhibit clear segregation with age. The $[\text{Fe}/\text{H}]$ gradients become slightly steeper with the increasing age of open clusters, as previously discussed in Donor et al. (2020). $[\text{Fe}/\text{H}]$ gradients are steeper than $[\text{Ce}/\text{H}]$ gradients in all age bins (see Table 3).

Gradients of $[\text{Ce}/\text{Fe}]$ ratio are shown in Figure 10; the best-fit slopes were computed segregating the cluster sample according to the same age bins as done for $[\text{Ce}/\text{H}]$ and

$[\text{Fe}/\text{H}]$. In general, younger open clusters show higher $[\text{Ce}/\text{Fe}]$ ratios than older clusters (blue circles) at a given galactocentric distance. For $R_{\text{GC}} < 15$ kpc, we find an increasing $[\text{Ce}/\text{Fe}]$ ratio with increasing R_{GC} , which is opposite to the behavior of the $[\text{Ce}/\text{H}]$ gradient. The $[\text{Ce}/\text{Fe}]$ gradients for the open clusters with age < 1 Gyr, $1 \text{ Gyr} \leq \text{age} \leq 2$ Gyr, and age > 2 Gyr are 0.018 ± 0.007 , 0.027 ± 0.007 , and $0.035 \pm 0.007 \text{ dex kpc}^{-1}$, respectively. We find that the slopes of the linear fits in the $[\text{Ce}/\text{Fe}]-R_{\text{GC}}$ plane are very similar, becoming just modestly steeper with increasing open cluster age, with the $[\text{Ce}/\text{Fe}]$ gradient changing by $\sim +0.009 \text{ dex kpc}^{-1} \text{ Gyr}^{-1}$. This change is approximately equal to the gradient uncertainties (≈ 0.007 , see Table 3). We noted that the $[\text{Ce}/\text{Fe}]$ ratios for the open clusters NGC 6791, NGC 2243, and Trumpler 5 are consistent with the $[\text{Ce}/\text{Fe}]$ linear gradient shown by the old open clusters.

Magrini et al. (2018) also found an overall increase in the $[\text{Ce}/\text{Fe}]$ ratio with galactocentric distance using the open cluster sample from the GAIA-ESO survey, but they do not present a gradient. More recently, Tautvaišienė et al. (2021) estimated the $[\text{Ce}/\text{Fe}]$ gradient for a sample of 424 thin-disk stars spanning ages from 0.1 to 9.5 Gyr, and R_{GC} from 5.5 to 11.8 kpc. For all thin-disk stars, they found a $[\text{Ce}/\text{Fe}]$ gradient of $+0.015 \pm 0.007 \text{ dex kpc}^{-1}$, a very similar gradient to our estimate using the entire open cluster sample ($+0.014 \pm 0.007 \text{ dex kpc}^{-1}$). Tautvaišienė et al. (2021) did not calculate the $[\text{Ce}/\text{Fe}]$ gradient binned by age. The $[\text{Ce}/\text{Fe}]$ gradient obtained here is also in line with the recent results for Ba from Spina et al. (2021). The latter study found that the $[\text{Ba}/\text{Fe}]$ ratio increases with galactocentric distance for $5 \text{ kpc} < R_{\text{GC}} < 12 \text{ kpc}$. The dependence of the production of heavy s-process elements (such as Ce) on metallicity can explain the increase in the $[\text{Ce}/\text{Fe}]$ ratio with increasing R_{GC} . AGB stars from regions with lower metallicity (outer disk) show greater Ce yields than AGB stars with high metallicity (inner disk) (Cristallo et al. 2015; Karakas & Lugaro 2016).

Only two clusters in our sample (Berkeley 20 and Berkeley 29) have galactocentric distances greater than 15 kpc; gradient determinations for the outer disk using this sample would not be meaningful. However, these two distant open clusters have similar ages and $[\text{Ce}/\text{H}]$ and $[\text{Ce}/\text{Fe}]$ ratios, which may indicate constant $[\text{Ce}/\text{H}]$ and $[\text{Ce}/\text{Fe}]$ gradients for the old open clusters in the outer disk.

5. Conclusions

The evolution and gradient of s-process elements in the Galactic disk are still not well defined due to considerable distance and age uncertainties for field stars and small and heterogeneous open cluster samples. Large spectroscopic surveys such as GAIA-ESO (Gilmore et al. 2012), GALAH (De Silva et al. 2015), as well as APOGEE (Majewski et al. 2017) are changing this scenario by increasing significantly the number of homogeneous chemical abundance measurements for s-process elements for field stars and to a lesser extent open clusters. Along these lines, we determined the abundance of the s-process-dominated element cerium for 218 stars belonging to 42 open clusters from the OCCAM/APOGEE DR16 survey. The Ce abundances obtained in this study allowed us to determine details of the chemical evolution of Ce in the Galactic disk and its relationship with metallicity. In addition, we estimated the Ce gradient and its change over time for the studied open cluster sample. Our results can be summarized as follows.

²⁶ The residual (the difference between the observed value and that predicted by the linear fit, $[\text{Ce}/\text{H}] - [\text{Ce}/\text{H}]_{\text{fit}}$, in the cluster R_{GC}) for each open cluster using the fit from its respective age group.

[Ce/Fe]–[Fe/H] plane. The $[\text{Ce}/\text{Fe}]$ ratio increases as the metallicity decrease for the different age sets of the open clusters, with a possible change in the trend for $[\text{Fe}/\text{H}] < -0.2$ for the old open clusters. Our results also indicate that older open clusters have lower $[\text{Ce}/\text{Fe}]$ ratio values than the young open clusters in the same metallicity range. The $[\text{Ce}/\text{Fe}]$ ratios of our sample, which was derived from the APOGEE spectra in the near-infrared, are slightly overabundant if one compares with literature Ce abundances from high-resolution optical spectroscopy obtained for dwarf and giant stars in the field. This overabundance of Ce in the open cluster population relative to field stars is in line with results from the literature from other s-process elements that also find similar behavior. Age may contribute to such differences, field stars being systematically older than open clusters.

Chemical evolution of Ce. Metallicity segregates open clusters in the $[\text{Ce}/\text{X}]$ –age plane, with X being H, Fe, or α -elements (O, Mg, Si, or Ca). Open clusters with lower metallicity show $[\text{Ce}/\text{Fe}]$ and $[\text{Ce}/\alpha]$ ratios higher than those with high metallicity at a given age. For ages < 4 Gyr, the Ce abundance increases with decreasing age of the open clusters. In other words, younger open clusters show higher $[\text{Ce}/\text{Fe}]$ and $[\text{Ce}/\alpha]$ ratios than older open clusters with similar metallicities. For ages > 4 Gyr, the trends of the $[\text{Ce}/\text{Fe}]$ and $[\text{Ce}/\alpha]$ ratios with age are approximately constant, but our sample is small in this age range.

$[\text{Ce}/\alpha]$ as a stellar chemical clock. The abundance ratio between s-process and α -elements has emerged in the literature as the main candidate for the universal chemical clock for stars. The examination of such a ratio in the open clusters provides an excellent opportunity to test this hypothesis. Our results indicate that the relationship of the $[\text{Ce}/\alpha]$ ratio with age is not the same across the Galactic disk, which is possibly due to the dependence of AGB yields on metallicity.

Ce abundance gradients. For clusters with $R_{\text{GC}} < 15$ kpc, we find negative (-0.070 ± 0.007 dex kpc^{-1}) and positive (0.014 ± 0.007 dex kpc^{-1}) gradients for the $[\text{Ce}/\text{H}]$ and $[\text{Ce}/\text{Fe}]$ ratios, respectively. Age segregates the open clusters in the $[\text{Ce}/\text{H}]$ – R_{GC} and $[\text{Ce}/\text{Fe}]$ – R_{GC} planes, a different behavior when compared to the metallicity gradient, which does not show this separation. The linear gradients in $[\text{Ce}/\text{H}]$ and $[\text{Ce}/\text{Fe}]$ shift to smaller values in $[\text{Ce}/\text{H}]$ and $[\text{Ce}/\text{Fe}]$ for the older open clusters. We also find that the $[\text{Ce}/\text{H}]$ and $[\text{Ce}/\text{Fe}]$ gradients are approximately constant with cluster age. The $[\text{Ce}/\text{Fe}]$ gradient becomes slightly steeper over time, changing by $\sim +0.009$ dex kpc^{-1} Gyr^{-1} , marginally greater than the gradient uncertainties (~ 0.007).

Overall, our results indicate a strong dependence of the Ce abundance on metallicity and age. Iron (^{56}Fe) nuclei work as seeds for the s-process, hence the close relationship between metallicity and the s-process. The production of heavy s-process elements, such as Ce, is lower in high-metallicity AGB stars, due to the lower number of neutrons per iron-56 seed nucleus, which favors the production of the light s-process elements (Sr, Y, and Zr) (Cristallo et al. 2009, 2011, 2015; Karakas & Lattanzio 2014; Karakas & Lugaro 2016). The nature of the behavior of increasing abundance of heavy s-process elements with decreasing age for open clusters is not fully understood (Baratella et al. 2021). The relationship between $[\text{Ce}/\text{Fe}]$ and age for open clusters may be related to the delay in the enrichment of some Ce-producing stars, such as $1.5 M_{\odot}$ stars, which takes a few gigayears to add AGB products to the interstellar medium. However, AGB models indicate low

yields of heavy s-process elements for very low-mass stars (Cristallo et al. 2015; Karakas & Lugaro 2016). The formation of an extended ^{13}C pocket induced by mixing processes can increase Ce production (e.g., Battino et al. 2021) and may explain its overabundance in the young open clusters, as pointed out by Maiorca et al. (2011).

J.V.S.S. acknowledges the PCI/CNPQ program under the grant 301863/2021-0.

P.M.F., J.D., and J.O. acknowledge support for this research from the National Science Foundation (AST-1311835 & AST-1715662). P.M.F. also acknowledges some of this work was performed at the Aspen Center for Physics, which is supported by National Science Foundation grant PHY-1607611.

S.R.M. acknowledges support from NSF grant AST-1909497.

D.A.G.H. acknowledges support from the State Research Agency (AEI) of the Spanish Ministry of Science, Innovation and Universities (MCIU) and the European Regional Development Fund (FEDER) under grant AYA2017-88254-P.

Funding for the Sloan Digital Sky Survey IV has been provided by the Alfred P. Sloan Foundation, the U.S. Department of Energy Office of Science, and the Participating Institutions. SDSS-IV acknowledges support and resources from the Center for High-Performance Computing at the University of Utah. The SDSS website is www.sdss.org.

SDSS-IV is managed by the Astrophysical Research consortium for the Participating Institutions of the SDSS Collaboration including the Brazilian Participation Group, the Carnegie Institution for Science, Carnegie Mellon University, the Chilean Participation Group, the French Participation Group, Harvard Smithsonian Center for Astrophysics, Instituto de Astrofísica de Canarias, The Johns Hopkins University, Kavli Institute for the Physics and Mathematics of the Universe (IPMU)/University of Tokyo, Lawrence Berkeley National Laboratory, Leibniz Institut für Astrophysik Potsdam (AIP), Max-Planck-Institut für Astronomie (MPIA Heidelberg), Max-Planck Institut für Astrophysik (MPA Garching), Max-Planck-Institut für Extraterrestrische Physik (MPE), National Astronomical Observatory of China, New Mexico State University, New York University, University of Notre Dame, Observatório Nacional/MCTI, The Ohio State University, Pennsylvania State University, Shanghai Astronomical Observatory, United Kingdom Participation Group, Universidad Nacional Autónoma de México, University of Arizona, University of Colorado Boulder, University of Oxford, University of Portsmouth, University of Utah, University of Virginia, University of Washington, University of Wisconsin, Vanderbilt University, and Yale University.

This research made use of following Python packages: matplotlib (Hunter 2007), Numpy (Harris et al. 2020), Scipy (Virtanen et al. 2020), Emcee (Foreman-Mackey et al. 2013).

Facility: Sloan (APOGEE).

Software: matplotlib (Hunter 2007), Numpy (Harris et al. 2020), Scipy (Virtanen et al. 2020).

Appendix Ce Abundances for All Cluster Stars

Line-by-line Ce abundances for all cluster stars used in our analysis.

Table 4
Line-by-line Ce Abundances and Atmospheric Parameters (T_{eff} , $\log g$, ξ , and $[\text{Fe}/\text{H}]$) for All Cluster Stars

Cluster	ID	S/N	T_{eff} (K)	$\log g$	ξ (km s $^{-1}$)	$[\text{Fe}/\text{H}]$	Ce II absorption lines (\AA)							$\langle A(\text{Ce}) \rangle \pm \sigma$
							15277.6	15784.8	15977.1	16327.3	16376.5	16595.2	16722.6	
Basel 11b	2M05581816+2158437	296	4759	2.67	1.23	−0.00	1.88	...	1.97	1.97	...	1.94 ± 0.05
Berkeley 17	2M05202118+3035544	166	4746	2.77	1.14	−0.13	...	1.69	1.74	...	1.72 ± 0.04
Berkeley 17	2M05202905+3032414	98	4708	2.99	0.83	−0.15	...	1.61	1.70	...	1.66 ± 0.06
Berkeley 17	2M05203121+3035067	172	4773	2.79	1.13	−0.16	...	1.63	1.55	1.75	...	1.64 ± 0.10
Berkeley 17	2M05203650+3030351	396	4340	2.20	1.18	−0.15	1.61	1.59	...	1.60 ± 0.01
Berkeley 17	2M05203799+3034414	333	4202	2.10	1.15	−0.15	...	1.63	1.53	1.57	...	1.58 ± 0.05
Berkeley 17	2M05204143+3036042	168	4772	2.77	1.16	−0.20	...	1.56	1.51	1.68	...	1.58 ± 0.09
Berkeley 17	2M05204488+3038020	180	4753	2.72	1.18	−0.20	...	1.64	1.66	...	1.65 ± 0.01
Berkeley 19	2M05240941+2937217	110	4381	2.03	1.23	−0.32	...	1.73	1.51	...	1.67	1.65	...	1.64 ± 0.09
Berkeley 20	2M05323895+0011203	68	4313	1.99	1.21	−0.40	...	1.51	1.36	1.45	...	1.44 ± 0.08
Berkeley 29	2M06531569+1656176	56	4635	2.62	1.11	−0.45	...	1.62	1.35	...	1.42	1.46 ± 0.14
Berkeley 43	2M19152201+1115544	544	4715	2.85	1.13	0.03	2.00	2.04	...	2.02 ± 0.03
Berkeley 53	2M20554232+5106153	217	4695	2.66	1.14	−0.06	1.74	1.95	1.74	...	1.89	1.93	...	1.85 ± 0.10
Berkeley 53	2M20554936+5106545	367	4362	2.17	1.19	−0.09	1.79	...	1.81	1.91	...	1.84 ± 0.06
Berkeley 53	2M20554998+5102175	94	4669	2.64	1.18	−0.08	1.90	1.88	...	1.89 ± 0.01
Berkeley 53	2M20555767+5103206	276	4915	2.88	1.19	−0.12	...	1.99	1.79	...	1.97	1.89	...	1.91 ± 0.09
Berkeley 53	2M20555959+5100466	55	4937	3.00	1.12	−0.10	1.85	1.80	...	1.83 ± 0.04
Berkeley 53	2M20561018+5102389	320	4820	2.71	1.21	−0.06	...	1.94	1.88	1.97	...	1.93 ± 0.05
Berkeley 66	2M03040128+5846422	60	4893	2.78	1.24	−0.18	1.71	1.81	...	1.76 ± 0.07
Berkeley 66	2M03042797+5845042	59	4907	2.84	1.22	−0.14	...	1.72	1.85	...	1.77	1.78 ± 0.07
Berkeley 98	2M22423502+5222084	93	4495	2.67	1.12	0.00	1.80	...	1.81	1.76	1.76	1.78 ± 0.03
BH 211	2M17021851+4109170	398	4789	2.86	1.16	0.19	...	2.09	2.03	2.09	...	2.07 ± 0.03
Collinder 220	2M10260294+5755255	836	4804	2.55	1.35	−0.08	1.92	2.08	...	2.00 ± 0.11
Czernik 21	2M05263726+3600404	150	4978	2.93	1.15	−0.32	...	1.74	1.56	1.58	...	1.63 ± 0.10
Czernik 21	2M05264047+3602191	114	4878	2.86	1.12	−0.33	...	1.57	1.61	1.70	...	1.63 ± 0.07
Czernik 30	2M07310830+0956359	170	4286	1.94	1.23	−0.39	...	1.62	1.47	1.46	...	1.52 ± 0.09
Czernik 30	2M07311590+0955415	113	4440	2.22	1.24	−0.40	1.42	1.56	...	1.49 ± 0.10
FSR 0394	2M22545788+5844048	157	4728	2.76	1.17	−0.10	...	1.76	1.93	1.88	1.86 ± 0.09
FSR 0394	2M22550718+5842026	149	4918	2.77	1.22	−0.09	...	1.80	1.93	1.86 ± 0.09
IC 166	2M01522953+6151427	126	4807	2.83	1.16	−0.09	1.86	1.86
IC 1369	2M21115265+4744571	238	4953	2.78	1.29	−0.04	1.91	1.96	...	1.94 ± 0.04
IC 1369	2M21120996+4744158	267	4919	2.83	1.22	−0.07	1.89	1.97	...	1.93 ± 0.06
IC 1369	2M21121345+4745256	385	4968	2.55	1.50	−0.12	1.79	1.98	...	1.88 ± 0.13
King 2	2M00510072+5810562	232	4062	1.66	1.24	−0.36	...	1.61	1.50	1.51	...	1.53	...	1.53 ± 0.05
King 5	2M03142548+5247355	619	4209	1.79	1.23	−0.16	...	1.86	1.76	1.85	...	1.82 ± 0.06
King 7	2M03590443+5148003	519	4895	2.45	1.50	−0.15	2.01	1.98	2.02	...	2.00 ± 0.02
King 7	2M03591013+5145193	291	4706	2.17	1.48	−0.18	1.99	...	1.90	1.93	...	1.94 ± 0.05
King 7	2M03591747+5147014	522	4317	1.86	1.33	−0.13	1.94	...	1.89	1.96	...	1.93 ± 0.04
King 7	2M03592828+5148425	409	4848	2.40	1.51	−0.18	2.04	2.04	...	2.04 ± 0.00
NGC 188	2M00415197+8527070	409	4609	2.74	1.12	0.11	1.87	1.86	...	1.87 ± 0.01
NGC 188	2M00422570+8516219	272	4562	2.91	1.02	0.09	1.86	1.79	...	1.83 ± 0.05
NGC 188	2M00444460+8532163	243	4791	3.31	1.00	0.11	1.56	1.69	1.62 ± 0.09
NGC 188	2M00472975+8524140	362	4661	2.97	1.03	0.13	1.59	1.86	...	1.72 ± 0.19
NGC 188	2M00512176+8512377	207	4665	3.04	1.05	0.08	1.86	1.89	1.88 ± 0.02
NGC 188	2M00533497+8511145	373	4650	3.02	0.94	0.09	1.81	...	1.81
NGC 188	2M00533572+8520583	280	4517	2.81	1.06	0.10	1.87	1.76	...	1.82 ± 0.08

Table 4
(Continued)

Cluster	ID	S/N	T_{eff} (K)	$\log g$	ξ (km s $^{-1}$)	[Fe/H]	Ce II absorption lines (\AA)							$\langle A(\text{Ce}) \rangle \pm \sigma$
							15277.6	15784.8	15977.1	16327.3	16376.5	16595.2	16722.6	
NGC 188	2M00541152+8515231	460	4621	2.72	1.12	0.09	1.82	1.82	1.82	1.82 ± 0.00
NGC 188	2M00543664+8501152	483	4637	2.78	1.14	0.10	1.87	1.91	1.89 ± 0.03
NGC 188	2M00571844+8510288	373	4573	2.72	1.13	0.10	1.80	1.95	1.88 ± 0.11
NGC 752	2M01562163+3736084	1137	4814	3.00	1.06	-0.04	1.78	1.92	...	1.85 ± 0.10
NGC 1193	2M03060593+4421203	112	4660	2.57	1.16	-0.33	...	1.38	1.54	1.46 ± 0.11
NGC 1193	2M03060808+4423347	90	4718	2.69	1.10	-0.34	1.56	1.56
NGC 1245	2M03141134+4709173	388	4481	2.28	1.21	-0.14	1.71	...	1.90	1.81	...	1.81 ± 0.10
NGC 1798	2M05112446+4740027	259	4399	2.13	1.20	-0.27	1.65	1.73	1.74	...	1.71 ± 0.05
NGC 1798	2M05113666+4741482	200	4656	2.45	1.22	-0.27	...	1.82	1.66	1.76	...	1.75 ± 0.08
NGC 1798	2M05113768+4742329	138	4762	2.55	1.21	-0.27	...	1.62	1.69	1.66 ± 0.05
NGC 1798	2M05114006+4739238	182	4692	2.52	1.18	-0.24	...	1.80	1.73	1.80	...	1.78 ± 0.04
NGC 1798	2M05114134+4740406	115	4821	2.70	1.19	-0.25	...	1.66	1.59	...	1.80	1.68 ± 0.11
NGC 1798	2M05114626+4743422	181	4603	2.40	1.22	-0.26	1.70	...	1.62	...	1.75	1.67	...	1.68 ± 0.05
NGC 1907	2M05280420+3519163	366	4941	2.89	1.22	-0.08	...	1.93	1.92	1.94	...	1.93 ± 0.01
NGC 2158	2M06070155+2401470	79	4898	2.80	1.26	-0.21	1.76	1.86	1.74	1.71	...	1.77 ± 0.07
NGC 2158	2M06070415+2409180	56	4957	2.84	1.26	-0.18	1.81	1.84	...	1.83 ± 0.02
NGC 2158	2M06071494+2407517	143	4464	2.35	1.22	-0.22	1.70	...	1.59	...	1.76	1.76	...	1.70 ± 0.08
NGC 2158	2M06071696+2402007	72	4920	2.86	1.23	-0.19	1.76	1.81	1.66	1.74 ± 0.08
NGC 2158	2M06071787+2405542	164	4342	2.17	1.22	-0.20	1.69	...	1.83	1.80	1.84	1.79 ± 0.07
NGC 2158	2M06071913+2400148	71	4974	2.90	1.21	-0.21	1.78	1.87	1.65	1.75	...	1.76 ± 0.09
NGC 2158	2M06072041+2407463	62	4903	2.81	1.21	-0.24	...	1.75	1.62	1.68	...	1.68 ± 0.07
NGC 2158	2M06072443+2400524	65	4877	2.89	1.22	-0.23	1.71	1.85	...	1.78 ± 0.10
NGC 2158	2M06072624+2409568	75	4990	3.04	1.14	-0.21	...	1.80	1.64	...	1.88	1.80	...	1.78 ± 0.10
NGC 2158	2M06072907+2402151	87	4912	2.98	1.20	-0.18	1.66	...	1.81	...	1.76	1.88	...	1.78 ± 0.09
NGC 2158	2M06072918+2408185	81	4989	3.03	1.21	-0.21	1.73	1.69	1.75	...	1.72 ± 0.03
NGC 2158	2M06073636+2405001	74	4989	3.06	1.20	-0.19	1.77	1.88	1.81	1.82 ± 0.06
NGC 2158	2M06073917+2409098	73	4970	2.98	1.21	-0.17	...	1.79	1.76	1.74	...	1.76 ± 0.03
NGC 2158	2M06073998+2403546	79	4962	3.00	1.18	-0.22	...	1.74	1.88	1.81 ± 0.10
NGC 2158	2M06074162+2405540	67	4864	2.91	1.21	-0.23	...	1.82	1.70	1.76 ± 0.08
NGC 2158	2M06074272+2402514	74	4982	3.03	1.26	-0.26	...	1.78	1.73	1.76 ± 0.04
NGC 2158	2M06075243+2403561	77	4968	3.05	1.17	-0.22	1.79	1.77	...	1.78 ± 0.01
NGC 2204	2M06151360-1841498	148	4937	2.83	1.25	-0.28	1.70	1.70
NGC 2204	2M06152142-1835512	264	4655	2.54	1.25	-0.24	1.76	1.81	1.79	...	1.79 ± 0.03
NGC 2204	2M06153043-1838239	163	4695	2.67	1.18	-0.26	1.70	1.61	...	1.66 ± 0.06
NGC 2204	2M06153192-1839369	322	4428	2.18	1.24	-0.28	1.61	1.68	1.78	1.75	...	1.70 ± 0.08
NGC 2204	2M06153696-1836091	133	4999	2.92	1.25	-0.26	1.61	...	1.61
NGC 2204	2M06154970-1837393	271	4473	2.29	1.24	-0.27	1.76	1.80	...	1.78 ± 0.03
NGC 2243	2M06292300-3117299	189	4967	2.77	1.32	-0.51	1.32	...	1.31	...	1.38	1.32 ± 0.05
NGC 2243	2M06292939-3115459	140	4979	2.80	1.30	-0.46	1.47	1.48	1.38	...	1.44 ± 0.06
NGC 2243	2M06293009-3116587	293	4576	2.31	1.24	-0.51	1.34	...	1.31	...	1.40	1.41	...	1.37 ± 0.05
NGC 2243	2M06293525-3115470	60	4951	3.07	1.26	-0.45	1.36	1.36
NGC 2243	2M06293565-3117110	124	4969	2.78	1.28	-0.45	1.38	...	1.46	1.42 ± 0.06
NGC 2243	2M06294150-3114360	172	4678	2.56	1.16	-0.44	1.35	1.45	1.52	...	1.44 ± 0.09
NGC 2243	2M06294583-3115382	231	4928	2.74	1.30	-0.46	1.34	1.37	1.49	...	1.40 ± 0.08
NGC 2243	2M06295100-3114428	100	4886	3.36	0.71	-0.41	1.58	1.58
NGC 2304	2M06550345+1759521	217	4770	2.76	1.15	-0.14	1.85	...	1.82	...	1.87	1.87	...	1.85 ± 0.02

Table 4
(Continued)

Cluster	ID	S/N	T_{eff} (K)	$\log g$	ξ (km s $^{-1}$)	[Fe/H]	Ce II absorption lines (Å)							$\langle A(\text{Ce}) \rangle \pm \sigma$
							15277.6	15784.8	15977.1	16327.3	16376.5	16595.2	16722.6	
NGC 2324	2M07035166+0106381	350	4902	2.74	1.24	−0.20	1.73	...	1.82	...	1.86	1.91	...	1.83 ± 0.08
NGC 2324	2M07040031+0058168	217	4431	2.06	1.29	−0.16	1.78	...	1.84	...	1.94	1.86	...	1.86 ± 0.07
NGC 2420	2M07380545+2136507	219	4842	2.97	1.12	−0.19	1.75	1.58	1.74	...	1.69 ± 0.10
NGC 2420	2M07380627+2136542	413	4691	2.71	1.16	−0.24	1.63	1.68	...	1.65 ± 0.04
NGC 2420	2M07381507+2134589	1076	4091	1.69	1.22	−0.24	1.63	...	1.79	1.74	...	1.72 ± 0.08
NGC 2420	2M07381549+2138015	322	4898	2.91	1.16	−0.19	1.65	1.63	1.74	...	1.67 ± 0.06
NGC 2420	2M07382148+2135050	221	4870	3.00	1.14	−0.18	1.67	...	1.72	1.78	...	1.72 ± 0.06
NGC 2420	2M07382195+2135508	270	4896	2.93	1.15	−0.14	1.48	...	1.83	1.66 ± 0.25
NGC 2420	2M07382670+2128514	130	4888	2.96	1.18	−0.16	...	1.76	1.76	...	1.79	1.81	...	1.78 ± 0.02
NGC 2420	2M07382696+2138244	315	4836	2.81	1.18	−0.17	1.76	...	1.71	...	1.78	1.83	...	1.77 ± 0.05
NGC 2420	2M07382984+2134509	229	4781	2.93	1.11	−0.19	1.61	1.64	1.61	...	1.62 ± 0.02
NGC 2420	2M07383760+2134119	269	4912	2.94	1.15	−0.18	1.66	...	1.64	...	1.66	1.85	...	1.70 ± 0.10
NGC 2682	2M08504964+1135089	342	4726	3.00	1.08	0.04	1.71	...	1.73	1.81	...	1.75 ± 0.05
NGC 2682	2M08510839+1147121	171	4946	3.46	1.04	0.04	1.71	1.88	...	1.80 ± 0.12
NGC 2682	2M08511269+1152423	768	4736	2.82	1.11	0.01	1.77	...	1.64	...	1.74	1.87	...	1.76 ± 0.09
NGC 2682	2M08511704+1150464	371	4698	2.95	1.08	−0.03	...	1.82	1.62	...	1.65	1.78	...	1.72 ± 0.10
NGC 2682	2M08511897+1158110	393	4948	3.38	1.09	0.02	...	1.84	1.59	1.76	...	1.73 ± 0.13
NGC 2682	2M08512156+1146061	645	4757	3.04	1.08	0.05	...	1.79	1.72	1.81	...	1.77 ± 0.05
NGC 2682	2M08512280+1148016	1001	4728	2.78	1.16	0.04	...	1.92	1.65	...	1.81	1.81	...	1.80 ± 0.11
NGC 2682	2M08512618+1153520	785	4747	2.81	1.13	0.00	1.72	1.82	...	1.77 ± 0.07
NGC 2682	2M08512898+1150330	949	4696	2.77	1.13	0.02	1.71	1.82	...	1.76 ± 0.08
NGC 2682	2M08513577+1153347	205	4932	3.41	1.01	0.02	...	1.80	1.52	1.69	...	1.67 ± 0.14
NGC 2682	2M08513938+1151456	390	4898	3.32	1.06	0.03	...	1.82	1.59	1.64	...	1.68 ± 0.12
NGC 2682	2M08514234+1150076	270	4783	3.15	1.07	0.03	1.64	1.84	...	1.74 ± 0.14
NGC 2682	2M08514235+1151230	668	4716	2.97	1.10	0.00	1.76	1.77	1.62	1.78	...	1.73 ± 0.08
NGC 2682	2M08514388+1156425	950	4751	2.80	1.16	0.01	1.62	1.89	1.73	1.80	...	1.76 ± 0.11
NGC 2682	2M08514507+1147459	466	4778	3.06	1.10	0.01	1.70	1.77	...	1.74 ± 0.05
NGC 2682	2M08515952+1155049	996	4748	2.81	1.13	0.00	1.72	1.78	...	1.75 ± 0.04
NGC 2682	2M08521097+1131491	667	4563	2.76	1.07	0.04	1.78	1.78	1.68	1.79	...	1.76 ± 0.05
NGC 2682	2M08521656+1119380	1058	4326	2.31	1.10	0.01	...	1.75	1.73	1.75	...	1.74 ± 0.01
NGC 2682	2M08521856+1144263	503	4708	2.81	1.14	0.02	1.79	...	1.67	...	1.80	1.76	...	1.76 ± 0.06
NGC 2682	2M08522003+1127362	260	4975	3.50	1.06	0.02	...	1.76	1.50	1.82	...	1.69 ± 0.17
NGC 2682	2M08522636+1141277	197	4980	3.54	0.85	0.03	1.58	1.78	...	1.68 ± 0.14
NGC 4337	2M12235244-5806564	191	4885	3.14	1.12	0.23	2.06	1.91	2.02	2.00	2.00 ± 0.06
NGC 4337	2M12235665-5807252	159	4857	3.17	1.09	0.26	2.00	2.10	...	2.05 ± 0.07
NGC 4337	2M12240101-5807554	585	4286	2.26	1.19	0.22	1.86	2.07	1.96	2.10	2.00 ± 0.11
NGC 4337	2M12240488-5805099	168	4880	3.23	1.09	0.31	1.99	2.17	...	2.08 ± 0.13
NGC 4337	2M12240586-5807152	156	4906	3.18	1.09	0.19	2.01	...	2.01
NGC 4337	2M12241575-5808502	200	4889	3.16	1.12	0.22	1.84	2.00	...	1.92 ± 0.11
NGC 6705	2M18505494-0616182	394	4650	2.84	1.02	0.12	1.99	...	2.05	2.00	...	2.01 ± 0.03
NGC 6705	2M18505944-0612435	376	4870	3.15	0.83	0.09	2.09	...	1.89	2.07	...	2.02 ± 0.11
NGC 6705	2M18510092-0614564	457	4783	2.89	1.09	0.10	2.00	2.03	...	2.01 ± 0.02
NGC 6705	2M18510399-0620414	455	4717	2.72	1.20	0.16	...	1.99	1.94	2.07	...	2.00 ± 0.07
NGC 6705	2M18510626-0615134	438	4775	2.80	1.18	0.16	1.93	2.07	...	2.00 ± 0.10
NGC 6705	2M18510661-0612442	453	4758	2.88	1.14	0.17	...	2.04	2.06	2.12	...	2.07 ± 0.04
NGC 6705	2M18510786-0617119	350	4778	3.00	1.10	0.05	2.05	2.05

Table 4
(Continued)















Cluster	ID	S/N	T_{eff} (K)	$\log g$	ξ (km s $^{-1}$)	[Fe/H]	Ce II absorption lines (Å)							$\langle A(\text{Ce}) \rangle \pm \sigma$
							15277.6	15784.8	15977.1	16327.3	16376.5	16595.2	16722.6	
NGC 6705	2M18511048-0615470	475	4749	2.87	1.12	0.09	2.09	...	2.08	1.98	...	2.05 \pm 0.06
NGC 6705	2M18511452-0616551	297	4811	3.06	1.02	0.11	2.06	2.09	...	2.08 \pm 0.02
NGC 6705	2M18511571-0618146	465	4731	2.74	1.21	0.16	1.98	2.01	1.91	...	2.07	1.98	...	1.99 \pm 0.06
NGC 6791	2M19203005+3750191	64	4470	2.80	1.08	0.35	2.09	...	2.11	...	2.15	2.12 \pm 0.03
NGC 6791	2M19203485+3746298	66	4448	2.67	1.06	0.36	2.04	...	2.10	...	2.10	2.08 \pm 0.03
NGC 6791	2M19203784+3745249	41	4400	2.82	0.92	0.34	2.17	2.17
NGC 6791	2M19203934+3748048	77	4212	2.45	1.09	0.30	...	2.03	2.06	2.05	2.03	2.04 \pm 0.02
NGC 6791	2M19204517+3744339	45	4356	2.76	0.75	0.40	2.21	2.06	...	2.13 \pm 0.11
NGC 6791	2M19205287+3745331	67	4474	2.80	1.06	0.36	2.04	2.04
NGC 6791	2M19205368+3750236	58	4483	2.79	1.05	0.41	2.04	...	2.04
NGC 6791	2M19205530+3743152	124	4189	2.44	1.00	0.34	1.98	2.03	...	2.00 \pm 0.04
NGC 6791	2M19205629+3744334	63	4443	2.72	1.07	0.39	2.11	...	2.06	2.00	...	2.06 \pm 0.06
NGC 6791	2M19210052+3750188	67	4429	2.98	0.75	0.28	2.15	2.23	2.19 \pm 0.06
NGC 6791	2M19210086+3745339	69	4387	2.64	1.10	0.39	...	2.14	2.02	2.17	2.16	2.12 \pm 0.07
NGC 6791	2M19210112+3742134	137	4156	2.37	1.08	0.32	1.97	1.93	2.15	2.02 \pm 0.12
NGC 6791	2M19210426+3747187	134	4061	2.00	1.15	0.33	2.09	...	1.95	2.15	2.04	2.06 \pm 0.08
NGC 6791	2M19210483+3741036	98	4480	2.84	0.86	0.41	2.13	2.25	2.08	2.15 \pm 0.09
NGC 6791	2M19210604+3752049	79	4474	2.98	0.99	0.35	...	1.93	2.20	...	2.06 \pm 0.19
NGC 6791	2M19210629+3744596	67	4438	2.73	1.02	0.36	1.98	2.07	2.07	2.04 \pm 0.05
NGC 6791	2M19211007+3750008	103	4435	2.85	1.04	0.32	2.16	2.12	2.14 \pm 0.03
NGC 6791	2M19211300+3743005	63	4439	2.91	1.00	0.36	2.14	2.02	...	2.08 \pm 0.08
NGC 6791	2M19203266+3746221	113	4257	2.53	1.10	0.37	2.13	2.23	2.10	2.15 \pm 0.07
NGC 6791	2M19204356+3747019	112	4255	2.41	1.14	0.30	2.05	...	1.90	...	2.01	1.91	2.12	2.00 \pm 0.09
NGC 6791	2M19204965+3744077	118	4461	2.64	1.11	0.35	1.99	...	2.00	2.00 \pm 0.01
NGC 6791	2M19205784+3747067	102	4486	2.95	1.06	0.37	2.13	1.88	...	2.00 \pm 0.18
NGC 6791	2M19205874+3743130	109	4449	2.67	1.10	0.38	2.05	...	2.03	2.10	...	2.06 \pm 0.04
NGC 6791	2M19210086+3746396	117	4450	2.60	1.14	0.35	1.79	...	2.00	1.90 \pm 0.15
NGC 6791	2M19211725+3743187	118	4400	2.56	1.12	0.40	2.01	2.25	2.22	2.16 \pm 0.13
NGC 6811	2M19373462+4624098	435	4944	3.03	1.14	-0.02	...	1.85	1.82	1.92	...	1.86 \pm 0.05
NGC 6819	2M19404803+4008085	324	4507	2.64	1.11	0.02	...	1.82	1.82	...	1.82 \pm 0.0
NGC 6819	2M19404965+4014313	223	4675	2.89	1.11	0.05	...	1.88	1.73	1.82	...	1.81 \pm 0.08
NGC 6819	2M19405020+4013109	237	4738	2.90	1.10	0.09	1.93	1.93	...	1.93 \pm 0.0
NGC 6819	2M19405601+4013395	141	4885	3.22	0.86	0.06	...	1.69	1.84	1.76 \pm 0.11
NGC 6819	2M19405797+4008174	288	4826	2.95	1.13	0.09	1.96	1.95	1.84	1.94	...	1.92 \pm 0.06
NGC 6819	2M19410524+4014042	130	4778	2.89	1.12	0.08	1.89	2.09	2.00	1.99 \pm 0.10
NGC 6819	2M19410622+4010532	135	4867	3.18	1.04	0.07	1.75	1.75	...	1.75 \pm 0.0
NGC 6819	2M19410858+4013299	249	4751	2.84	1.13	0.08	...	1.80	1.90	1.94	...	1.88 \pm 0.07
NGC 6819	2M19410926+4014436	257	4762	2.91	1.08	0.07	1.88	1.84	...	1.86 \pm 0.03
NGC 6819	2M19410991+4015495	148	4737	2.80	1.13	0.00	1.81	1.83	1.98	1.87 \pm 0.09
NGC 6819	2M19411102+4011116	370	4944	2.87	1.24	0.06	1.88	2.01	2.06	1.98 \pm 0.09
NGC 6819	2M19411115+4011422	305	4611	2.57	1.18	0.09	1.82	1.82	2.02	...	1.89 \pm 0.12
NGC 6819	2M19411279+4012238	188	4769	2.83	1.15	0.07	...	1.75	1.88	1.82 \pm 0.09
NGC 6819	2M19411345+4011561	171	4767	2.86	1.14	0.03	1.76	1.76
NGC 6819	2M19411355+4012205	260	4795	2.86	1.14	0.03	...	1.91	1.77	1.82	...	1.83 \pm 0.07
NGC 6819	2M19411476+4011008	281	4892	3.00	1.15	0.10	1.90	1.92	...	1.91 \pm 0.01
NGC 6819	2M19411564+4010105	133	4747	2.90	1.12	0.09	...	1.82	2.10	...	1.96 \pm 0.20

Table 4
(Continued)

Cluster	ID	S/N	T_{eff} (K)	$\log g$	ξ (km s $^{-1}$)	[Fe/H]	Ce II absorption lines (\AA)							$\langle A(\text{Ce}) \rangle \pm \sigma$
							15277.6	15784.8	15977.1	16327.3	16376.5	16595.2	16722.6	
NGC 6819	2M19411705+4010517	805	4014	1.72	1.21	−0.01	...	1.82	...	1.70	...	1.73	1.83	1.77 ± 0.06
NGC 6819	2M19411893+4011408	168	4659	2.87	1.09	0.03	...	1.75	1.68	...	1.84	1.85	...	1.78 ± 0.08
NGC 6819	2M19412136+4011002	132	4589	2.75	1.08	0.04	1.91	1.91
NGC 6819	2M19412147+4013573	251	4765	2.87	1.14	0.09	...	1.94	1.80	1.95	1.93	1.90 ± 0.07
NGC 6819	2M19412176+4012111	260	4582	2.75	1.13	0.06	...	1.84	1.78	1.88	...	1.83 ± 0.05
NGC 6819	2M19412245+4012033	133	4957	3.15	1.08	0.06	1.80	1.80
NGC 6819	2M19412658+4011418	347	4404	2.33	1.18	0.01	...	1.89	1.87	1.90	...	1.89 ± 0.02
NGC 6819	2M19412707+4012283	214	4525	2.66	1.10	0.04	...	1.89	1.84	1.80	...	1.84 ± 0.05
NGC 6819	2M19412915+4013040	185	4792	2.88	1.15	0.07	...	1.83	1.93	1.93	...	1.90 ± 0.06
NGC 6819	2M19412942+4014199	137	4670	2.88	1.08	0.05	...	1.86	1.85	...	1.83	1.86	...	1.85 ± 0.01
NGC 6819	2M19412953+4012210	270	4737	2.84	1.16	0.07	...	1.91	1.83	1.98	1.98	1.93 ± 0.07
NGC 6819	2M19413027+4015218	262	4774	2.87	1.15	0.06	...	1.89	1.80	1.84	...	1.84 ± 0.05
NGC 6819	2M19413330+4012349	261	4606	2.67	1.15	−0.00	...	1.73	1.70	1.75	...	1.73 ± 0.03
NGC 7789	2M23554966+5639180	279	4424	2.35	1.21	−0.00	1.83	1.96	1.74	1.84	...	1.84 ± 0.09
NGC 7789	2M23562953+5648399	319	4948	3.12	1.09	−0.03	...	1.87	1.88	...	1.88 ± 0.01
NGC 7789	2M23563930+5645242	310	4966	3.13	1.10	0.01	1.80	1.92	...	1.86 ± 0.08
NGC 7789	2M23564304+5650477	322	4929	3.09	1.12	0.02	1.91	1.93	...	1.92 ± 0.01
NGC 7789	2M23565751+5645272	685	4531	2.61	1.11	−0.00	1.87	1.92	1.88	1.90	...	1.89 ± 0.02
NGC 7789	2M23570895+5648504	290	4981	3.13	1.15	0.04	1.82	1.92	1.91	1.88	...	1.88 ± 0.04
NGC 7789	2M23571400+5640586	604	4472	2.49	1.15	−0.01	1.80	...	1.80	1.92	...	1.84 ± 0.07
NGC 7789	2M23571728+5645333	128	4992	3.18	1.14	−0.02	...	1.94	1.99	...	1.96 ± 0.04
NGC 7789	2M23571847+5650271	326	4879	2.98	1.13	−0.03	...	1.86	1.84	...	1.83	1.90	...	1.86 ± 0.03
NGC 7789	2M23573184+5641221	934	4352	2.27	1.17	−0.02	1.80	...	1.83	1.91	...	1.94	...	1.87 ± 0.07
NGC 7789	2M23573563+5640000	139	4948	3.16	1.09	0.02	...	1.99	1.97	...	1.98 ± 0.01
NGC 7789	2M23580015+5650125	687	4369	2.29	1.14	−0.05	1.75	1.88	...	1.82 ± 0.09
NGC 7789	2M23580275+5647208	289	4716	2.90	1.06	−0.02	1.75	1.91	1.96	...	1.87 ± 0.11
NGC 7789	2M23581471+5651466	713	4251	2.10	1.18	−0.03	1.78	1.83	1.82	1.81	...	1.95	...	1.84 ± 0.07
Ruprecht 147	2M19164574-1635226	999	4781	3.15	0.99	0.14	...	1.76	1.81	1.95	...	1.84 ± 0.10
SAI 116	2M11491181-6214125	400	4652	2.62	1.26	0.17	2.07	2.11	...	2.09 ± 0.03
SAI 116	2M11491918-6214038	358	4601	2.53	1.20	0.15	2.00	1.98	...	1.99 ± 0.01
Teutsch 84	2M17041246-4206305	107	4934	3.18	1.12	0.21	...	2.01	1.98	2.00 ± 0.02
Trumpler 5	2M06363859+0938525	127	4787	2.73	1.15	−0.43	1.41	1.33	...	1.37 ± 0.06
Trumpler 5	2M06364229+0925257	344	4286	1.96	1.21	−0.44	1.39	1.41	1.43	...	1.41 ± 0.02
Trumpler 5	2M06364741+0919364	95	4830	2.80	1.19	−0.44	1.36	1.36

Note. In the third column, we present the signal-to-noise ratio of the spectra.

ORCID iDs

J. V. Sales-Silva  <https://orcid.org/0000-0003-0636-7463>
 K. Cunha  <https://orcid.org/0000-0001-6476-0576>
 P. M. Frinchaboy  <https://orcid.org/0000-0002-0740-8346>
 D. A. García-Hernández  <https://orcid.org/0000-0002-1693-2721>
 S. R. Majewski  <https://orcid.org/0000-0003-2025-3147>
 T. Masseron  <https://orcid.org/0000-0002-6939-0831>
 R. P. Schiavon  <https://orcid.org/0000-0002-2244-0897>
 D. H. Weinberg  <https://orcid.org/0000-0001-7775-7261>
 R. L. Beaton  <https://orcid.org/0000-0002-1691-8217>
 H. Jönsson  <https://orcid.org/0000-0002-4912-8609>
 R. R. Lane  <https://orcid.org/0000-0003-1805-0316>
 A. Manchado  <https://orcid.org/0000-0002-3011-686X>
 C. Nitschelm  <https://orcid.org/0000-0003-4752-4365>
 S. Villanova  <https://orcid.org/0000-0001-6205-1493>

References

- Alvarez, R., & Plez, B. 1998, *A&A*, **330**, 1109
 Baratella, M., D'Orazi, V., Sheminova, V., et al. 2021, *A&A*, **653**, A67
 Battino, U., Lederer-Woods, C., Cseh, B., Denissenkov, P., & Herwig, F. 2021, *Univ*, **7**, 25
 Battino, U., Tattersall, A., Lederer-Woods, C., et al. 2019, *MNRAS*, **489**, 1082
 Battistini, C., & Bensby, T. 2016, *A&A*, **586**, A49
 Bensby, T., Feltzing, S., & Oey, M. S. 2014, *A&A*, **562**, A71
 Bisterzo, S., Travaglio, C., Gallino, R., Wiescher, M., & Käppeler, F. 2014, *ApJ*, **787**, 10
 Blanton, M. R., Bershad, M. A., Abolfathi, B., et al. 2017, *AJ*, **154**, 28
 Bowen, I. S., & Vaughan, A. H., J. 1973, *ApOpt*, **12**, 1430
 Burbidge, E. M., Burbidge, G. R., Fowler, W. A., & Hoyle, F. 1957, *RvMP*, **29**, 547
 Cantat-Gaudin, T., Anders, F., Castro-Ginard, A., et al. 2020, *A&A*, **640**, A1
 Casali, G., Spina, L., Magrini, L., et al. 2020, *A&A*, **639**, A127
 Casamiquela, L., Soubiran, C., Jofré, P., et al. 2021, *A&A*, **652**, A25
 Chen, Y. Q., & Zhao, G. 2020, *MNRAS*, **495**, 2673
 Cristallo, S., Piersanti, L., Straniero, O., et al. 2011, *ApJS*, **197**, 17
 Cristallo, S., Straniero, O., Gallino, R., et al. 2009, *ApJ*, **696**, 797
 Cristallo, S., Straniero, O., Piersanti, L., & Gobrecht, D. 2015, *ApJS*, **219**, 40
 Cunha, K., Smith, V. V., Hasselquist, S., et al. 2017, *ApJ*, **844**, 145
 da Silva, R., Porto de Mello, G. F., Milone, A. C., et al. 2012, *A&A*, **542**, A84
 De Silva, G. M., Freeman, K. C., Bland-Hawthorn, J., et al. 2015, *MNRAS*, **449**, 2604
 Delgado Mena, E., Moya, A., Adibekyan, V., et al. 2019, *A&A*, **624**, A78
 Djordjevic, J. O., Thompson, M. A., Urquhart, J. S., & Forbrich, J. 2019, *MNRAS*, **487**, 1057
 Donor, J., Frinchaboy, P. M., Cunha, K., et al. 2020, *AJ*, **159**, 199
 D'Orazi, V., Magrini, L., Randich, S., et al. 2009, *ApJL*, **693**, L31
 Feltzing, S., Howes, L. M., McMillan, P. J., & Stenker, E. 2017, *MNRAS*, **465**, L109
 Fishlock, C. K., Yong, D., Karakas, A. I., et al. 2017, *MNRAS*, **466**, 4672
 Foreman-Mackey, D., Hogg, D. W., Lang, D., & Goodman, J. 2013, *PASP*, **125**, 306
 Forsberg, R., Jönsson, H., Ryde, N., & Matteucci, F. 2019, *A&A*, **631**, A113
 Gallino, R., Arlandini, C., Busso, M., et al. 1998, *ApJ*, **497**, 388
 Gallino, R., Bisterzo, S., Straniero, O., Ivans, I. I., & Käppeler, F. 2006, *Mem. Soc. Astron. Italiana*, **77**, 786
 García Pérez, A. E., Allende Prieto, C., Holtzman, J. A., et al. 2016, *AJ*, **151**, 144
 García-Hernández, D. A., García-Lario, P., Plez, B., et al. 2006, *Sci*, **314**, 1751
 García-Hernández, D. A., Zamora, O., Yagüe, A., et al. 2013, *A&A*, **555**, L3
 Gilmore, G., Randich, S., Asplund, M., et al. 2012, *Msngr*, **147**, 25
 Grevesse, N., Asplund, M., & Sauval, A. J. 2007, *SSRv*, **130**, 105
 Gunn, J. E., Siegmund, W. A., Mannery, E. J., et al. 2006, *AJ*, **131**, 2332
 Gustafsson, B., Edvardsson, B., Eriksson, K., et al. 2008, *A&A*, **486**, 951
 Harris, C. R., Millman, K. J., van der Walt, S. J., et al. 2020, *Natur*, **585**, 357
 Holtzman, J. A., Shetrone, M., Johnson, J. A., et al. 2015, *AJ*, **150**, 148
 Horta, D., Ness, M. K., Rybizki, J., Schiavon, R. P., & Buder, S. 2021, *arXiv:2111.01809*
 Hunter, J. D. 2007, *CSE*, **9**, 90
 Jacobson, H. R., & Friel, E. D. 2013, *AJ*, **145**, 107
 Jílková, L., Carraro, G., Jungwiert, B., & Minchev, I. 2012, *A&A*, **541**, A64
 Jofré, P., Jackson, H., & Tucci Maia, M. 2020, *A&A*, **633**, L9
 Jönsson, H., Holtzman, J. A., Allende Prieto, C., et al. 2020, *AJ*, **160**, 120
 Käppeler, F., Gallino, R., Bisterzo, S., & Aoki, W. 2011, *RvMP*, **83**, 157
 Karakas, A. I., & Lattanzio, J. C. 2014, *PASA*, **31**, e030
 Karakas, A. I., & Lugaro, M. 2016, *ApJ*, **825**, 26
 Kharchenko, N. V., Piskunov, A. E., Schilbach, E., Röser, S., & Scholz, R. D. 2013, *A&A*, **558**, A53
 Lugaro, M., Herwig, F., Lattanzio, J. C., Gallino, R., & Straniero, O. 2003, *ApJ*, **586**, 1305
 Magrini, L., Spina, L., Randich, S., et al. 2018, *A&A*, **617**, A106
 Magrini, L., Vescovi, D., Casali, G., et al. 2021, *A&A*, **646**, L2
 Maiorca, E., Magrini, L., Busso, M., et al. 2012, *ApJ*, **747**, 53
 Maiorca, E., Randich, S., Busso, M., Magrini, L., & Palmerini, S. 2011, *ApJ*, **736**, 120
 Majewski, S. R., Schiavon, R. P., Frinchaboy, P. M., et al. 2017, *AJ*, **154**, 94
 Martínez-Medina, L. A., Gieles, M., Pichardo, B., & Peimbert, A. 2018, *MNRAS*, **474**, 32
 Masseron, T., Merle, T., & Hawkins, K. 2016, BACCHUS: Brussels Automatic Code for Characterizing High accUracY Spectra, Astronomical Source Code Library, ascl:1605.004
 Miglio, A., Chiappini, C., Mackereth, J. T., et al. 2021, *A&A*, **645**, A85
 Mishenina, T., Pignatari, M., Carraro, G., et al. 2015, *MNRAS*, **446**, 3651
 Mishenina, T. V., Pignatari, M., Korotin, S. A., et al. 2013, *A&A*, **552**, A128
 Misiriotis, A., Xilouris, E. M., Papamastorakis, J., Boumis, P., & Goudis, C. D. 2006, *A&A*, **459**, 113
 Nidever, D. L., Holtzman, J. A., Allende Prieto, C., et al. 2015, *AJ*, **150**, 173
 Nissen, P. E. 2015, *A&A*, **579**, A52
 Peña Suárez, V. J., Sales Silva, J. V., Katime Santrich, O. J., Drake, N. A., & Pereira, C. B. 2018, *ApJ*, **854**, 184
 Piersanti, L., Cristallo, S., & Straniero, O. 2013, *ApJ*, **774**, 98
 Pignatari, M., Gallino, R., Heil, M., et al. 2010, *ApJ*, **710**, 1557
 Plez, B. 2012, Turbospectrum: Code for spectral synthesis, Astronomical Source Code Library, ascl:1205.004
 Prantzos, N., Abia, C., Limongi, M., Chieffi, A., & Cristallo, S. 2018, *MNRAS*, **476**, 3432
 Reddy, A. B. S., Giridhar, S., & Lambert, D. L. 2012, *MNRAS*, **419**, 1350
 Reddy, A. B. S., Giridhar, S., & Lambert, D. L. 2013, *MNRAS*, **431**, 3338
 Reddy, B. E., Lambert, D. L., & Allende Prieto, C. 2006, *MNRAS*, **367**, 1329
 Reddy, B. E., Tomkin, J., Lambert, D. L., & Allende Prieto, C. 2003, *MNRAS*, **340**, 304
 Santrich, O. J. K., Pereira, C. B., & Drake, N. A. 2013, *A&A*, **554**, A2
 Smith, V. V., Bizyaev, D., Cunha, K., et al. 2021, *AJ*, **161**, 254
 Souto, D., Allende Prieto, C., Cunha, K., et al. 2019, *ApJ*, **874**, 97
 Souto, D., Cunha, K., Smith, V. V., et al. 2018, *ApJ*, **857**, 14
 Spina, L., Meléndez, J., Karakas, A. I., et al. 2018, *MNRAS*, **474**, 2580
 Spina, L., Nordlander, T., Casey, A. R., et al. 2020, *ApJ*, **895**, 52
 Spina, L., Ting, Y. S., De Silva, G. M., et al. 2021, *MNRAS*, **503**, 3279
 Tautvaišienė, G., Viscasillas Vázquez, C., Mikolaitis, Š., et al. 2021, *A&A*, **649**, A126
 Thielemann, F. K., Eichler, M., Panov, I. V., & Wehmeyer, B. 2017, *ARNPS*, **67**, 253
 van Raai, M. A., Lugaro, M., Karakas, A. I., García-Hernández, D. A., & Yong, D. 2012, *A&A*, **540**, A44
 Vescovi, D., Cristallo, S., Busso, M., & Liu, N. 2020, *ApJL*, **897**, L25
 Villanova, S., Carraro, G., Geisler, D., Monaco, L., & Assmann, P. 2018, *ApJ*, **867**, 34
 Virtanen, P., Gommers, R., Oliphant, T. E., et al. 2020, *NatMe*, **17**, 261
 Wilson, J. C., Hearty, F. R., Skrutskie, M. F., et al. 2019, *PASP*, **131**, 055001
 Yong, D., Carney, B. W., & Friel, E. D. 2012, *AJ*, **144**, 95
 Zasowski, G., Cohen, R. E., Chojnowski, S. D., et al. 2017, *AJ*, **154**, 198